Article

Interaction of Lherzolite Xenoliths with Basanite is not Isochemical: Evidence from Tumusun Volcano, Baikal Rift Zone

Marina A. Gornova [1], Vasiliy A. Belyaev [1], Anas A. Karimov [1, 2]*, Alexander B. Perepelov [1] and Sergei I. Dril [1]

[1] A.P. Vinogradov A.P. Institute of Geochemistry, Siberian Branch of Russian Academy of Sciences, 1A, Favorsky St., 664033, Irkutsk, Russia
[2] Institute of Earth's Crust, Siberian Branch of Russian Academy of Sciences, 128, Lermontova St., 664033, Irkutsk, Russia
* Correspondence: anas@igc.irk.ru; Tel.: +7(914)0141927

Abstract: To investigate the process and chemistry of reaction zone formation, we conducted detailed petrographic observations and major-trace element analysis of rocks and minerals of lherzolite xenoliths from basanites of Tumusun volcano (Baikal Rift Zone). The reaction zones gradually disappear from contact toward center of xenoliths. This indicates their formation as a result of lherzolite-basanite interaction. The influence of basanite melt on major-trace element composition of secondary minerals of reaction zones is notable only at distance up to 100-200 μm from the contact. The major-trace element composition of secondary clinopyroxenes from orthopyroxene reaction zone indicates their formation from a melt formed by dissolution of orthopyroxene and influenced by element diffusion from basanite melt. Inside xenoliths the secondary minerals have Mg# values equal to or higher than Mg# of primary minerals. The secondary clinopyroxenes inherit their depleted or enriched REE pattern from primary pyroxenes. The major-trace element variations in secondary clinopyroxenes testify melt heterogeneity. Secondary clinopyroxene has slightly higher LILE and similar abundances of other trace elements compared to unreacted part of clinopyroxene grain. This is consistent with model developed from experimental studies: due to the interaction with basanite, incongruent dissolution of orthopyroxene occurs to form a melt which circulates in lherzolite and leads to pyroxenes and spinel dissolution. Non-dissolved centers of minerals are homogenous and similar in major-trace element composition to primary minerals. The process of peridotite-basanite interaction is not isochemical: even the centers of large xenoliths become enriched in LILE.

Keywords: mantle xenolith; lherzolite; clinopyroxene; basanite; reaction rim; melt-peridotite interaction; trace elements

1. Introduction

The studies of mantle peridotite xenoliths from alkaline basalts allow reconstructing the processes operating in the Earth's mantle. These peridotites usually have reaction zones around their primary minerals. Several principal ways are discussed concerning the origin of the reaction zones. The mineral reaction zones apparently could be formed either in the mantle or during transporting by alkaline basalts. In mantle, the reaction zones originated as a result of metasomatic reactions [1,2], fluid-induced partial melting [3] or decompression partial melting [4]. During transportation and ascend to the surface, the reaction zones are formed due to interaction of xenoliths with the host alkaline basaltic magmas [5,6] or decompression partial melting [7].

The composition of lithospheric mantle beneath the Baikal Rift Zone and adjacent regions was studied by many authors [8–11]. The previous studies of peridotite xenoliths from basanite of Miocene Tumusun volcano found that the peridotites are fertile lherzolites exhibiting reaction rims around clinopyroxene and spinel [8,9]. The reaction rims

 doi:10.20944/preprints202302.0204.v1

of pyroxenes were interpreted as a result of mantle metasomatism induced by alkali-rich and water-poor fluids. We conducted the petrographic study of relatively large xenoliths that makes it possible to confirm the formation of reaction rims due to interaction between peridotites and basanites during ascend to the surface. The present study is mainly aimed to answer the question, does the major- and trace-element composition of minerals and rocks is changing in this process. This is essential for the further studies on mantle stage of peridotite evolution (e.g., partial melting and melt-rock interaction).

2. Geological position of Tumusun volcano

The Baikal Rift Zone is a system of several sedimentation basins and axial and off-rift volcanic areas (Figure 1a). The Cenozoic basaltic volcanism of South Baikal volcanic area is active for 35 Ma from Oligocene till Holocene, and some researchers related this volcanism to the action of a mantle plume [12]. The largest volcanic impulse at 21-15 Ma formed large lava plateau covered the Khamar-Daban Range [13,14]. The Cenozoic basaltic lavas erupted onto heterogenous crustal basement made of metamorphosed fragments of island arc and back-arc complexes [15] which comprise metamorphic Khamar-Daman terrain. The Khamar-Daman terrain consists of several series: Slyudyanka (metamorphosed volcanogenic and sedimentary rocks), Khangarul (metamorphosed greywackes, tuffs and carbonates), and Khamardaban (metamorphosed flysch sediments). The accumulation of sediments occurred at 500-700 Ma [16], and high-grade metamorphism took place 481-485 Ma [17]. The metamorphic rocks are extensively intruded by Paleozoic granitoids.

Preprints (www.preprints.org) | NOT PEER-REVIEWED | Posted: 13 February 2023 doi:10.20944/preprints202302.0204.v1

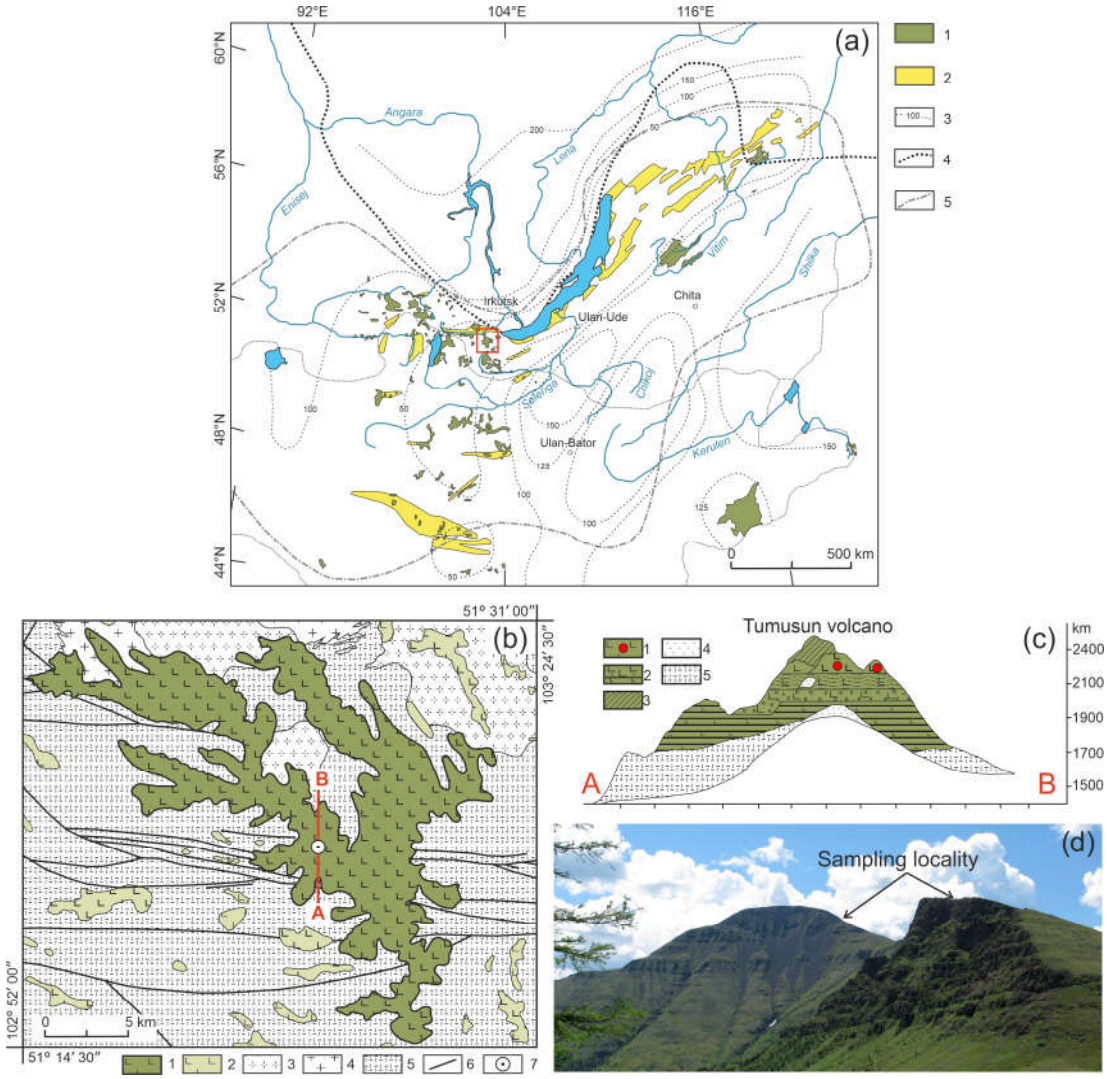

Figure 1. (**a**) Position of the Cenozoic volcanic areas in the Baikal Rift region [10]. 1 – Cenozoic volcanic areas; 2 – Cenozoic sedimentary basins; 3 – lithosphere thickness (in km); 4 – boundary of the Siberian Craton; 5 – boundary of distribution of anomalous mantle. The red square indicates the study area. (**b**) Geologic scheme of Tumusun area [18] compiled from State geological maps, sheets M48-I, M48-II, M48-VI, M48-VII. 1-2 – early-middle Miocene lavas of Tumusun plateau and other volcanic areas; 3 – early Paleozoic granites and granodiorites; 4 – late Proterozoic granites and granite gneisses; 5 – metamorphic basement (gneisses and schists); 6 – faults; 7 – position of Tumusun volcano. The red line is location of cross-section shown in c. (**c**) Cross-section of Tumusun volcano from [8]. 1 – flood basalts with xenolith material (marked by red circles); 2 – interlayering of basaltic lavas, lava conglomerates and sands; 3 – extrusive basalts; 4 – relics of tefrite basalts; 5 – metamorphic basement (gneisses and schists). (d) Landscape photograph of Tumusun volcano with sampling locality.

The Tumusun volcano (N 51°19′19″, E 103°14′48″) is located within Khamar-Daman Range at watershed between Tumusun and Utulik rivers. The Tumusun volcano is one of the largest erupting centers among the other Neogene basaltic areas of the Khamar-Daban Range (Figure 1b). The thickness of Tumusun lava flows is up to 500 m. The rock types are alkaline olivine basalt, hawaiite and, rarely, basanite. The volcanic sequence starts with voluminous eruptions of olivine basalt and hawaiite which comprise major lava plateau, and ends with formation of Tumusun neck composed of basanite. The lavas of volcanic plateau were dated by $^{40}Ar/^{39}Ar$ method at 16.9 ± 0.3 and 15.2 ± 0.2 Ma, and basanite of Tumusun neck was dated at 12.6 ± 0.3 Ma [14]. Therefore, basanite magmas erupted on final stages of Tumusun volcano development. As shown for other regions of South Baikal volcanic area, the basanite melts erupt later and have deeper source compared to that of

Preprints (www.preprints.org) | NOT PEER-REVIEWED | Posted: 13 February 2023 doi:10.20944/preprints202302.0204.v1

hawaiite melts [18]. The basanites of Tumusun volcano contain abundant mantle xenoliths of peridotite and pyroxenite. The peridotite xenoliths are the subject of present study. Among the studied collection, most of xenoliths are small (with size along three dimensions of 2-4 – 4-6 – 4-6 cm and one sample of only 1.5 cm in length), and only 3 are large (8-10 – 11-13 – 14-20 cm). At the contact between xenolith and basanite, there are discrete reaction zones in the xenoliths.

3. Analytical methods

The detailed petrographic observations were done with Olympus BX-51 optical microscope. The mineral identification was done with Tescan Mira 3 LMH scanning electron microscope (SEM) equipped with Oxford Ultim Max 40 energy-dispersive spectrometer (EDS). The mineral composition was acquired by electron probe micro analysis (EPMA) with JEOL JXA 8200 microprobe. Minerals were analyzed at accelerating voltage 20 kV, beam current 20 nA, probe diameter of 1 μm, counting time for background – 5 sec, analyte – 10 sec. The following standard reference materials (SRM) were used for calibration: albite (Na), olivine (Mg), pyrope (Al), diopside (Si, Ca), orthoclase (K), ilmenite (Ti), chromite (Cr), spessartine (Mn), trevorite (Fe, Ni), sphalerite (Zn), shcherbinaite (V). High-resolution electronic images of rock and mineral textures were obtained in backscattered electron mode.

Raman spectra of feldspars from reaction zones of pyroxenes and veinlets in interstitial space were obtained using WITec Alpha 300R confocal Raman spectrometer equipped with 532 nm laser and three gratings (300, 600, and 1800 grooves/mm). The laser was focused through 100x Zeiss objective.

Trace-element concentrations in primary silicate minerals (olivine, orthopyroxene, clinopyroxene) were determined in polished thick (~150-200 μm) sections by laser ablation inductively coupled plasma mass spectrometry (LA-ICP-MS) using a Analyte Excite analytic 193 ArF excimer laser (λ = 193 μm) with Helex II ablation cell and Agilent 7900 quadrupole ICP-MS. SRM NIST 612 were used for the initial calibration, SRM BCR-2G (basalt glass) was used to control the quality of analysis. All samples and standards were analyzed at the same measurement conditions: background measurement – 20 sec, sample analysis – 40 sec, laser beam diameter was 110 μm, energy 3.5 J/cm^2, pulse frequency – 10 Hz. The flow values of cooling gas, plasma-forming gas, and additive gas (Ar) were 16.0, 1.0, and 1.0 l/min respectively. Helium with a purity of 6.0 and a flow rate of 1.0 L/min was used as a carrier gas. The energy of the plasma was 1550 W. Element concentrations were calculated using the "Iolite 4" software [19,20]. ^{29}Si was used as an internal standard to calculate trace element abundances using SiO_2 abundances previously obtained by EPMA. The trace element abundances acquired by LA-ICP-MS were used to calculate whole-rock trace element composition.

Determination of trace element content in small mineral grains of pyroxenes from reaction zones, unreacted parts of pyroxene grains, and a number of primary pyroxenes were determined by secondary ion mass spectrometry (SIMS) Cameca IMS 4F at the Institute of Microelectronics of the Russian Academy of Sciences (Yaroslavl, Russia). Experiment conditions: focused primary beam of O_2^+ ions with energy of 14.5 keV, diameter of 20 μm, primary ion current of 8 nA. Each measurement included 5 cycles of signal accumulation, and the total time of analysis for one point was about 50 min. NIST 610 was used as calibration standard. The obtained signal was normalized to ^{30}Si and SiO_2 content determined by EPMA. Corrections for Gd, Yb, Eu, and Er were calculated according to the method [21]. Analyses of primary clino- and orthopyroxene performed by LA-ICP-MS and SIMS in the same samples yielded comparable results for both methods.

The concentrations of major elements in whole-rock samples were obtained by X-ray fluorescence (XRF) analysis using S8 Tiger spectrometer (Melitec). To perform the analysis, the rock powders (~ 110 mg weight) were fused with a mixture of lithium metaborate and lithium triborate with the addition of LiBr solution. The methodology is described in [22].

 doi:10.20944/preprints202302.0204.v1

The concentrations of trace elements in whole-rock samples were acquired by inductively coupled plasma mass spectrometry (ICP-MS) technique. Powdered samples (50 mg) were decomposed in a mixture of concentrated nitric and hydrofluoric acids (1:2) for 7 days at 110 °C. The analyses were performed using a Nexion300D (Perkin Elmer) quadrupole mass spectrometer.

EPMA, SEM, XRF and ICP-MS measurements were done at the Center for Isotope-Geochemical Studies of the Vinogradov Institute of Geochemistry, Siberian Branch of the Russian Academy of Sciences (IGC SB RAS, Irkutsk, Russia). LA-ICP-MS and Raman spectroscopy measurements were performed at the Center for Geodynamics and Geochronology of the Institute of the Earth's Crust, Siberian Branch of the Russian Academy of Sciences (IEC SB RAS, Irkutsk, Russia).

3. Results

3.1. Petrography

The studied xenoliths are spinel lherzolites. They have medium-grained protogranular textures. Olivine and orthopyroxene both have similar size of ~ 2 mm, but some samples contain rare larger (up to 6 mm) orthopyroxene. Clinopyroxene has smaller size (up to 1 mm). The pyroxenes do not contain exsolution lamellae. Spinel has irregular shape and occurs in an interstitial space.

The modal composition of peridotite xenoliths is: olivine (55.4-61.0 %), orthopyroxene (22.7-28.9 %), clinopyroxene (10.8-18.6 %), spinel (1.8-3.5 %). In all of the studied samples, the minerals exhibit reaction rims, and also thin veinlets in the interstitial space. Serpentine, amphibole, phlogopite, and other hydrous minerals are absent.

The olivine (Ol1) has a 50-100 μm wide reaction zone at the direct contact of xenolith with basanite. The reaction zone shows undulated border and is represented by olivine of different composition (Ol2) (Figure 2a).

Preprints (www.preprints.org) | NOT PEER-REVIEWED | Posted: 13 February 2023 doi:10.20944/preprints202302.0204.v1

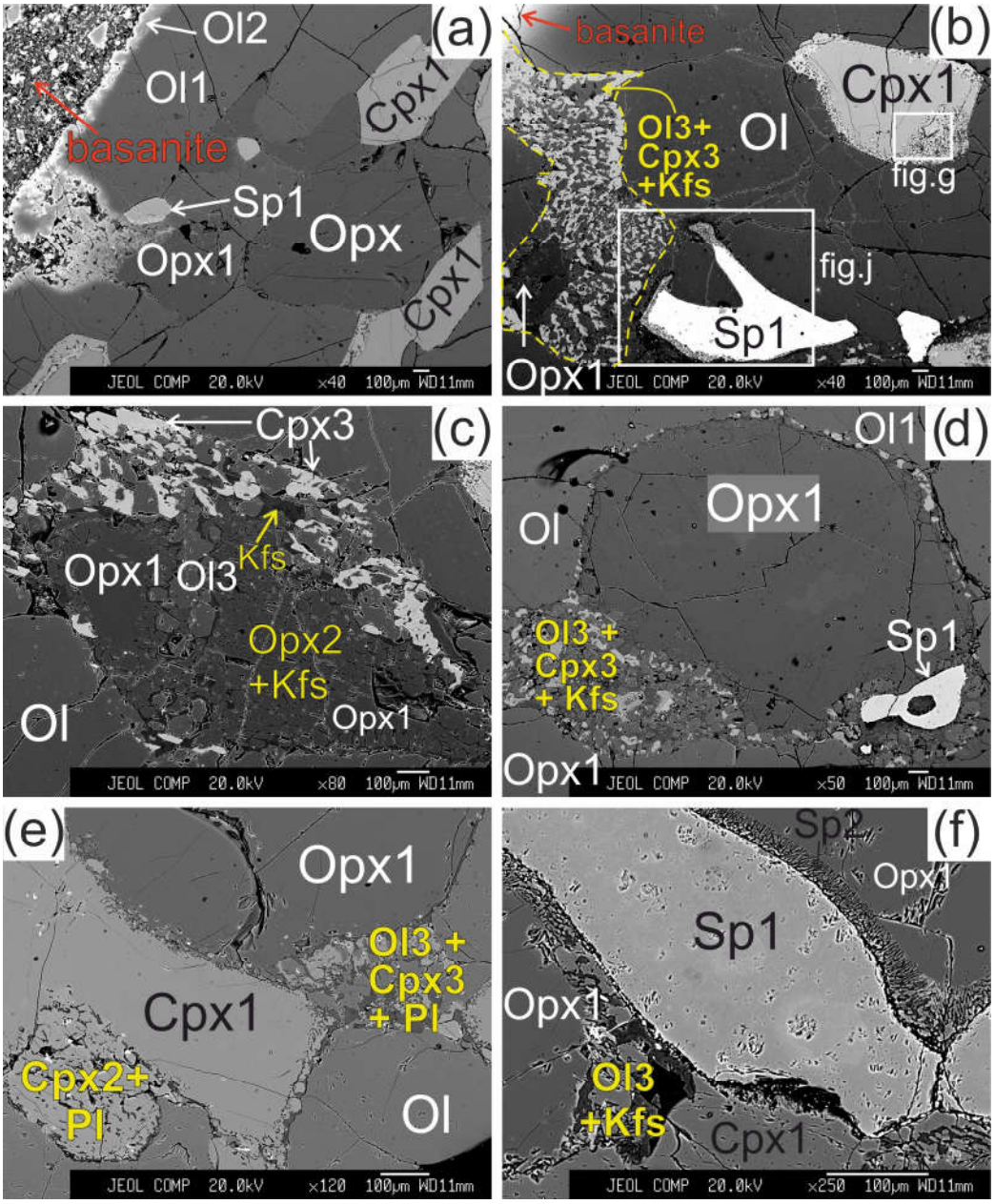

Figure 2. (a-f). Microstructural features of lherzolite xenolith of Tumusun volcano (back-scattered electron images). (**a**) Development of Ol2 rim after Ol1 at basanite/xenolith contact. Opx has wide reaction zone. Cpx has wider reaction zones on the grain boundaries oriented towards the contact. (**b**) Grain of orthopyroxene located close to basanite/xenolith contact and composed of non-reacted Opx1 and orthopyroxene reaction zone represented by secondary olivine (Ol3), clinopyroxene (Cpx3) and alkali feldspar (Kfs). Spinel (Sp1) has reaction zones at the contact with orthopyroxene. Clinopyroxene (Cpx1) has a reaction rim of different width. (**c**) Orthopyroxene reaction zone of second type, located at distance of 2 mm from the basanite/xenolith contact. Unreacted Opx1 is surrounded by secondary Opx2 intergrown with vermicular Kfs. These aggregates are cut by a chain of secondary Ol3. A smaller part of the reaction zone is made of Ol3, Cpx3 and Kfs. (**d**) Orthopyroxene grain with a thin reaction rim located at some distance from basanite/xenolith contact. (**e**) Zoned reaction zone (Ol3+Cpx3+Pl) irregularly developed around orthopyroxene inside xenolith. (**f**) Reaction zone of orthopyroxene (Ol3+Kfs) without secondary clinopyroxene, and reaction zone of spinel inside xenolith.

Preprints (www.preprints.org) | NOT PEER-REVIEWED | Posted: 13 February 2023 doi:10.20944/preprints202302.0204.v1

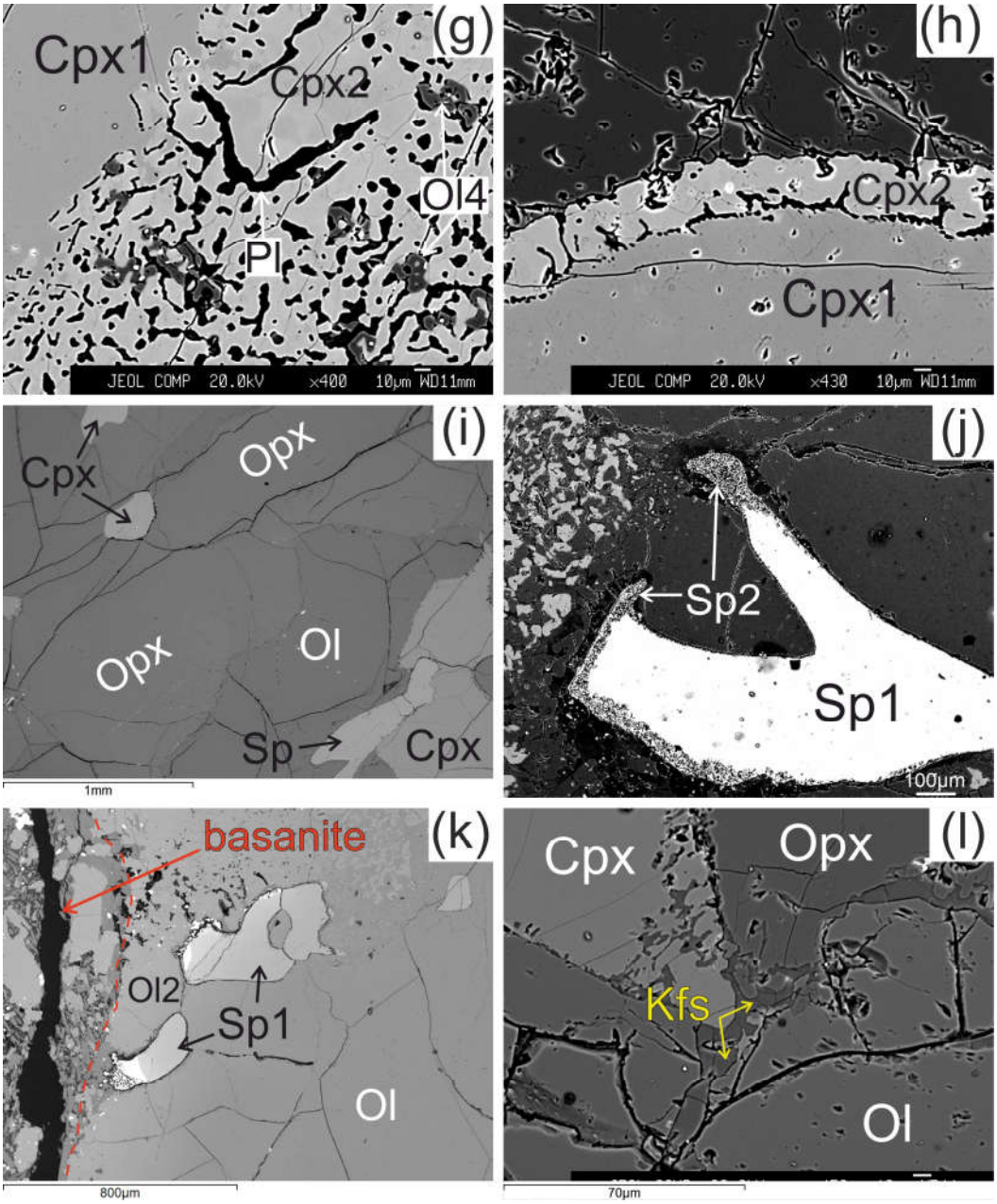

Figure 2. (g-l). Microstructural features of lherzolite xenoliths of Tumusun volcano. (**g**) Detailed image of clinopyroxene reaction zone composed of Cpx2 with inclusions of Ol4 (grey) and plagioclase (Pl, black) from Figure 2b. (**h**) Detailed image of clinopyroxene reaction rim from Figure 2f. (**i**) The center of large xenolith without reaction rims of pyroxenes and spinel. (**j**) Detailed image of spinel reaction zone from Figure 1b. The spinel reaction zone is composed of Kfs and secondary spinel (Sp2) intergrowth and is observed only next to the contact with the orthopyroxene reaction zone. (**k**) Reaction zones of spinel at basanite/xenolith contact. (**l**) Veinlet of K-feldspar inside xenolith. b-d, g, i – sample HD5; h – sample HD24/2; l – sample HD38; a – sample HD52; e – sample HD6/1; f – sample HD6/2.

The orthopyroxene (Opx) in direct contact with basanite has preserved only small areas of Opx1 surrounded by reaction zone with width up to hundreds of μm (see Figure 2b). The reaction rim of Opx1 is composed of intergrowth of small subhedral grains of olivine (Ol3) and clinopyroxene (Cpx3) and vermicular aggregates of alkali feldspar. The proportions of olivine, clinopyroxene and alkali feldspar in the reaction zone are ca. 50:40:10 %, respectively. Spinel (Sp3) and pentlandite is also found in these reaction zones. The border between reaction zone and orthopyroxene is sharp.

 doi:10.20944/preprints202302.0204.v1

Orthopyroxene at distance of ~2mm from basanite/xenolith contact also has preserved areas of Opx1 surrounded by complex reaction zone, consisting of two parts. A smaller part of the reaction zone is made of Ol3, Cpx3 and alkali feldspar, similar the reaction zones at basanite/xenolith contact. A larger part of the reaction zone is composed of small orthopyroxene grains (Opx2), divided by vermicular aggregates of alkali feldspar (see Figure 2c). This complex reaction zone is hereafter referred to as orthopyroxene reaction zone of second type.

In all samples, from basanite/xenolith contact toward the central part of xenoliths the orthopyroxene reaction zones become narrower (see Figure 2d). In central parts of largest xenoliths, the reaction zone of orthopyroxene is absent, or developed not around whole grain and similar to an interstitial aggregate (see Figure 2e, f, i, l). The reaction zones of orthopyroxene could have "zoning" – those parts of the reaction zone near to orthopyroxene are dominated by clinopyroxene, and those far from orthopyroxene are dominated by olivine (see Figure 2e). In the central parts of xenoliths, the reaction zone of orthopyroxene is made only of olivine and alkali feldspar (see Figure 2f).

The reaction zone around clinopyroxene (Cpx1) is formed by the rim of secondary clinopyroxene (Cpx2), which contains vermicular aggregates of plagioclase and less abundant small grains of olivine (Ol4) and spinel (Sp4). The transition from central part of clinopyroxene to the reaction rim is sharp (see Figure 2g, h). These clinopyroxene microtextures in xenoliths are described as "spongy" or "sieve" [4,5,9,23]. The width of reaction zone around clinopyroxene varies and is maximal at the basanite/xenolith contact and at contact with orthopyroxene reaction zone (see Figure 7l, 7i, 8c). In the closely located crystals of clinopyroxene, the width of reaction zone can be different (see Figure 8c). Toward the center of xenoliths, the width of clinopyroxene reaction zone become narrow (10-30 μm; Figure 2h) until its location only at certain crystal sides or complete disappearance (see Figure 2i, 2l, 7c).

The reaction zone of spinel (Sp1) is represented by intergrowth of small subhedral spinel (Sp2) and alkali feldspar. Such spinel microtexture was described as "sieve" texture [5,23]. It is developed either at basanite/xenolith contact or at contact with orthopyroxene reaction zone or feldspar veinlets (see Figure 2j, k). In other cases, the reaction zone of spinel is absent. This is observed at margins or in central parts of xenoliths.

In central parts of xenoliths there are thin (up to 10 μm) veinlets of alkali feldspar, located between grains of minerals which does not have reaction zones (see Figure 2l).

3.2. Mineral composition

Hereafter we use the term primary mineral, meaning the mineral without a reaction rim.

Primary olivine (Ol) is homogenous and have the same composition at margins and in the centers of xenoliths (Figure 3, Electronic Supplementary Table S1). The central parts of olivine grain (Ol1) rimned by Ol2 have the same composition as primary olivine. Olivine has the composition common for the fertile mantle lherzolites, and on Mg# – NiO the composition points are located within the mantle array (Figure 3). Olivine of reaction rims (Ol2) has notably lower Mg# (0.73-0.78) and NiO (0.13-0.16 wt. %) and higher CaO (0.31-0.46 wt.%), compared to grain cores (Mg# 0.91, 0.38 wt. % NiO, 0.08 wt. % CaO) (Figure 3, sample HD-52, Electronic Supplementary Table S1). Ol2 is similar to olivine phenocrysts from basanite. Ol3 from orthopyroxene reaction zone near basanite/xenolite contact has low Mg# (0.78-0.81), relatively low NiO (0.1-0.18 wt. %) and relatively high CaO (0.22-0.28 wt. %), i.e., similar in composition to olivine phenocrysts in basanite. Within a single reaction zone, over a distance of ~500 μm from basanite contact inward xenoliths, there is a growth in Mg# in Ol3 until Mg# became similar to that in primary olivine. At the same time, NiO is lower and CaO is higher in Ol3 compared to the composition of primary olivine (Figure 3, samples HD38, HD52, delineated by dashed line). In central parts of xenoliths, orthopyroxene reaction zones are narrow and their Ol3 has composition virtually similar to that of primary olivine (Figure 3, Electronic Supplementary Table S1).

Preprints (www.preprints.org) | NOT PEER-REVIEWED | Posted: 13 February 2023 doi:10.20944/preprints202302.0204.v1

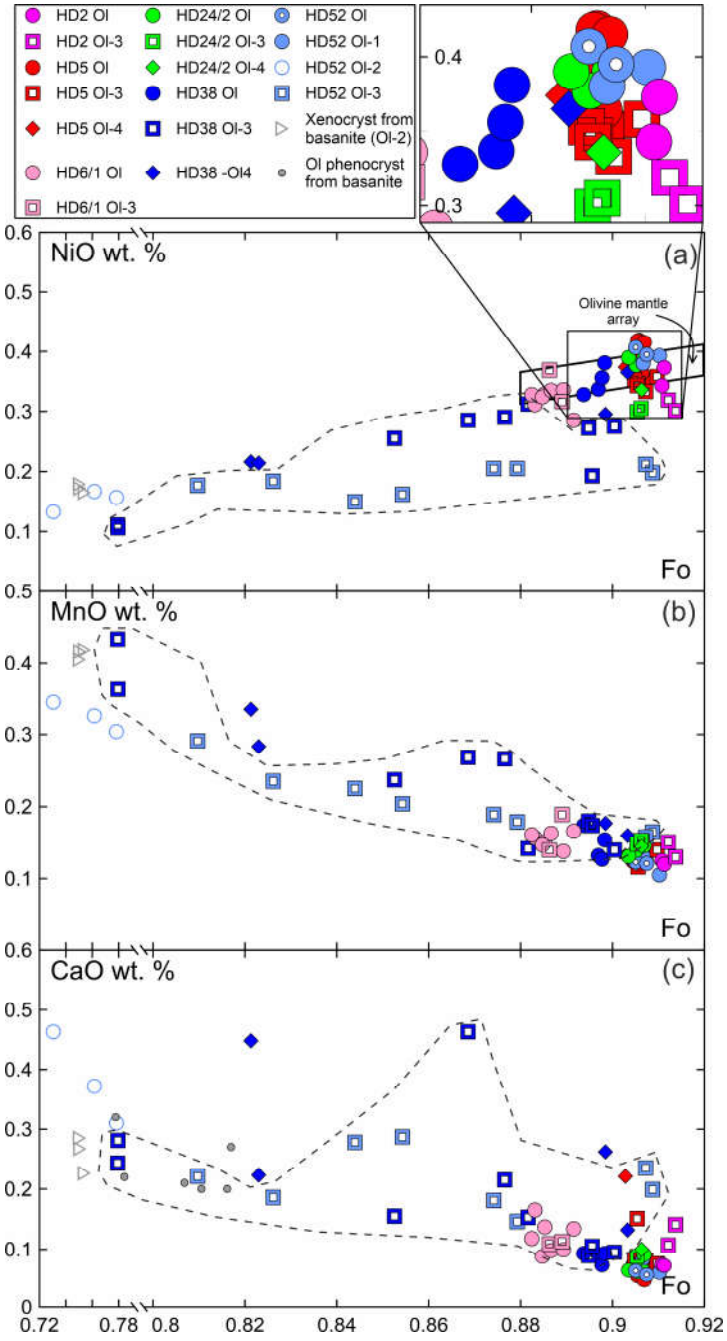

Figure 3. Composition of olivine from Tumusun lherzolite xenoliths. (**a**) NiO-Fo, (**b**) MnO-Fo, (**c**) CaO-Fo. Ol – primary olivine, Ol1 – core of olivine with reaction zim at basanite/xenolith contact, Ol2 – secondary olivine from reaction rim of Ol1, Ol3 – secondary olivine from reaction rim of Opx1, Ol4 – secondary olivine from reaction rim of Cpx1. The dashed line show compositions of Ol3 from reaction zone of Opx1 located at basanite/xenolith contact.

In reaction zones of clinopyroxene at basanite/xenolith contact, Ol4 has low Mg# (0.82) and NiO (0.21 wt. %) and high CaO (0.22-0.45 wt. %) (see Figure 3, sample HD38; Electronic Supplementary Table S1). In clinopyroxene reaction zones inside the xenoliths, Ol 4 has Mg# close to that of primary olivine, while NiO is similar to or lower and CaO is close to or higher than that of Ol1 (see Figure 3; Electronic Supplementary Table S1).

Primary orthopyroxene (Opx) is homogeneous enstatite. At xenolith margins, non-reacted Opx1 is also homogenous and have composition similar to that of primary orthopyroxene from centers of xenoliths. Opx2 from rare reaction zone (Opx2 + Kfs; see Figure 2c) has lower Al_2O_3, higher Mg# and CaO abundance (Figure 4; Electronic Supplementary Table S1).

Preprints (www.preprints.org) | NOT PEER-REVIEWED | Posted: 13 February 2023 doi:10.20944/preprints202302.0204.v1

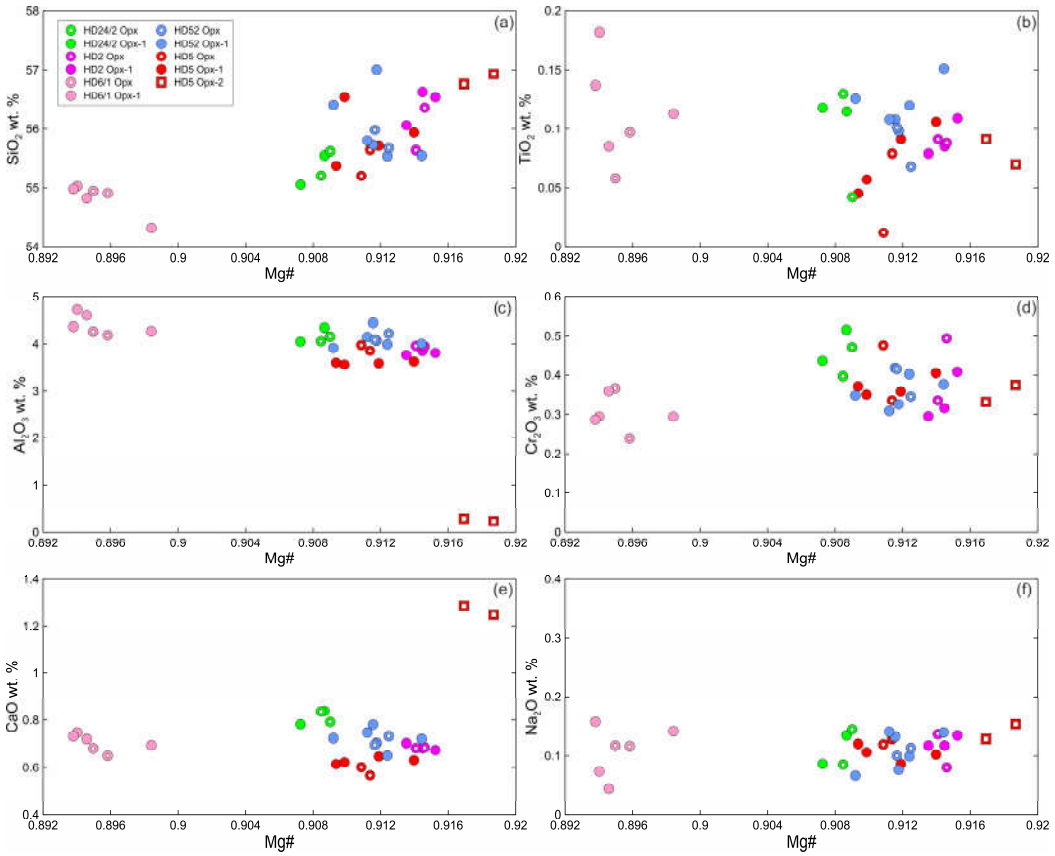

Figure 4. Composition of orthopyroxene from Tumusun lherzolite xenoliths. (a) SiO_2-Mg# (Mg#=Mg/(Mg+Fe^{2+})), (b) TiO_2-Mg#, (c) Al_2O_3-Mg#, (d) Cr_2O_3-Mg#, (e) CaO-Mg#, (f) Na_2O-Mg#. Opx – primary Opx without reaction zone, Opx1 – center of orthopyroxene with reaction zone, Opx2 – secondary orthopyroxene from second-type reaction zone of Opx1.

The primary clinopyroxene (Cpx) is diopside. Non-reacted parts of clinopyroxenes (Cpx1) surrounded by reaction rim are homogenous and have the same composition as primary clinopyroxenes without reaction rim (Figure 5, Electronic Supplementary Table S1). The secondary clinopyroxene (Cpx2) of reaction rims Cpx1 is diopside (Electronic Supplementary Table S1). Inside xenoliths, Cpx2 has lower Al_2O_3, Al^{VI}/Al^{IV} ratio, and Na_2O and higher SiO_2 and CaO compared to Cpx1. Mg#, TiO_2 and Cr_2O_3 in Cpx2 vary from levels as in Cpx1 to higher values (Figure 5). In outer rim of a clinopyroxene grain that is in immediate contact with basanite, Cpx2 has low Mg#, Al_2O_3, Na_2O and high TiO_2 and CaO and is similar in composition to clinopyroxene phenocrysts from basanite (Figure 5, sample HD38, delineated by dashed line). Cpx2 from internal rim of the same grain has composition similar to that of Cpx2 located farther from basanite/xenolith contact (Figure 5).

Preprints (www.preprints.org) | NOT PEER-REVIEWED | Posted: 13 February 2023 doi:10.20944/preprints202302.0204.v1

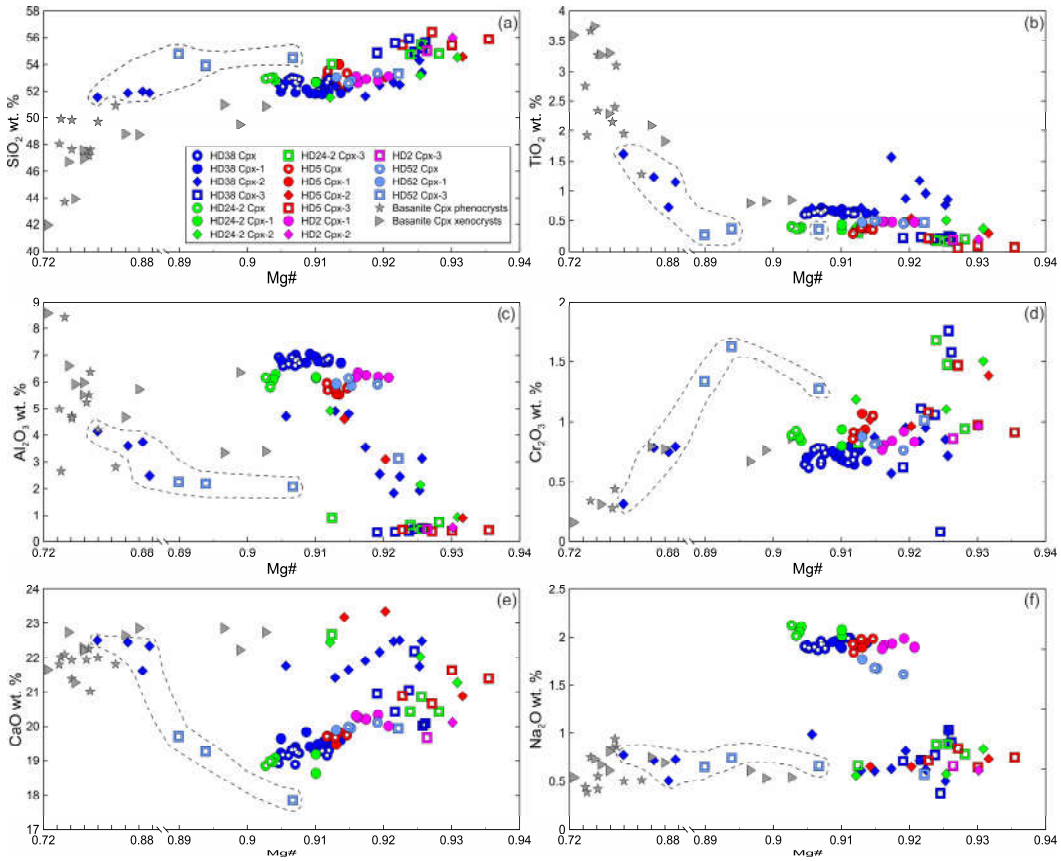

Figure 5. Composition of clinopyroxene from Tumusun lherzolite xenoliths. (**a**) SiO_2-Mg#, (**b**) TiO_2-Mg#, (**c**) Al_2O_3-Mg#, (**d**) Cr_2O_3-Mg#, (**e**) CaO-Mg#, (**f**) Na_2O-Mg#. Cpx – primary Cpx without reaction rim, Cpx1 – core of clinopyroxene with reaction zone, Cpx2 – secondary clinopyroxene from reaction zone of Cpx1, Cpx3 – secondary clinopyroxene from reaction zone of Opx1. The dashed line show compositions of secondary clinopyroxenes at basanite/xenolith contact.

Cpx3 from orthopyroxene reaction zones is augite (Electronic Supplementary Table S1). Composition of Cpx3 varies and depends on the position relative to basanite/xenolith contact. At first 100 μm from the contact, Cpx3 has lower Mg#, Al_2O_3, Na_2O, similar or lower CaO and TiO_2, and higher SiO_2 and Cr_2O_3 compared to primary clinopyroxene (see Figure 5, sample HD52, delineated by dashed line). At distance more than 100 μm from the contact, Cpx3 has higher Mg#, SiO_2, CaO, and lower Al_2O_3, TiO_2, Na_2O compared to Cpx1 (see Figure 5). Therefore, all secondary clinopyroxenes have less Al_2O_3 and Na_2O abundances then primary Cpx.

Primary chromium spinel is homogenous within a single sample. Secondary spinel from reaction zones of spinel (Sp2) and orthopyroxene (Sp3) exhibits higher Cr#, TiO_2, MnO, V_2O_5 and lower Mg# and NiO, compared to primary spinel (Electronic Supplementary Table S1).

Feldspar in reaction zones of orthopyroxene and spinel, as well as in veinlets between mineral grains is alkali feldspar (Figure 6a, Electronic Supplementary Table S1). Feldspar in reaction zones of clinopyroxene is plagioclase. Close to the basanite/xenolith contact, leucite is present in reaction zones of pyroxenes (Electronic Supplementary Table S1).

Raman spectra of feldspar from orthopyroxene reaction zones as well as from veinlets in interstitial space resemble those of sanidine (Figure 6b). Raman spectra of feldspar from clinopyroxene reaction zones correspond to that of anorthite (see Figure 6b).

Preprints (www.preprints.org) | NOT PEER-REVIEWED | Posted: 13 February 2023 doi:10.20944/preprints202302.0204.v1

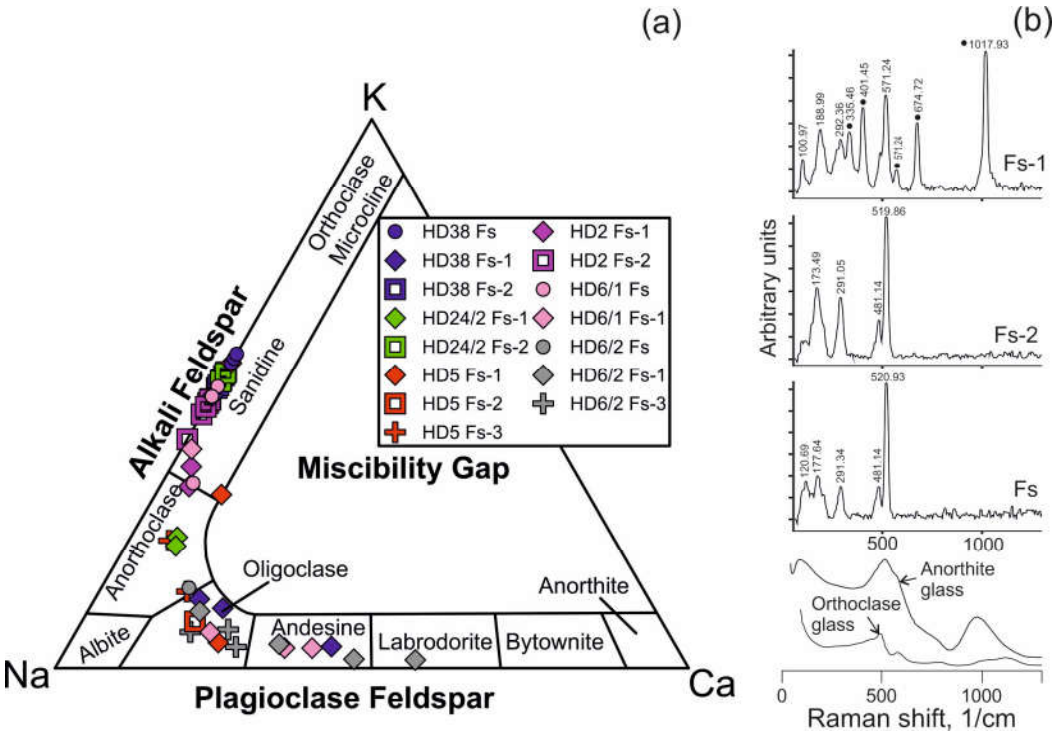

Figure 6. (**a**) Compositions of feldspar from Tumusun lherzolite xenoliths on ternary classification diagram. Fs – feldspar from veinlets in interstitial space, Fs-1 – feldspar from clinopyroxene reaction zones, Fs-2 – feldspar from orthopyroxene reaction zones, Fs-3 – feldspar from spinel reaction zones. (**b**) Raman spectra of feldspars from Tumusun lherzolite xenoliths. The spectrum of Fs-1 is influenced by signal of Cpx2 forming tight intergrowth with feldspar, and clinopyroxene Raman bands are marked by circles. Raman spectra of glasses of anorthite and orthoclase compositions [24] are shown for comparison.

3.3. Whole-rock major and trace element composition

The major and trace element whole-rock composition is listed in Table 1. In three largest xenoliths, marginal and central parts have been analyzed. The peridotites possess abundances of SiO_2, MgO, Al_2O_3, CaO, TiO_2 similar to that of primitive mantle. The marginal parts of xenoliths have evidently higher concentrations of K_2O and Na_2O compared to central parts, while the difference in other oxides is within analytical uncertainty. Small xenoliths, as well as margins of large xenoliths, have high K_2O and Na_2O, as pointed out earlier [9].

The rocks are characterized by two types of normalized trace element patterns – depleted and enriched. In the depleted type, the trace elements show decrease in normalized abundances toward most incompatible elements (Figure 7a), but have maxima of Rb, Ba, K, Pb, Sr, and minima of Nb, Zr, Hf, Ti. The enriched rock type exhibits increase in most incompatible elements, and multi-element plots demonstrate maximum of K and minimum Nb, while anomalies of Pb, Sr, Zr, Hf, Ti can be either positive or negative, or lack (Figure 7b-f). In general, in marginal parts of xenoliths the trace element pattern is similar to that of the central parts, but the marginal parts have higher abundances of LILE. In addition, the marginal part of sample HD6 shows higher LREE-MREE (Figure 7a-c). All studied small xenoliths demonstrate enriched trace-element patterns.

Preprints (www.preprints.org) | NOT PEER-REVIEWED | Posted: 13 February 2023 doi:10.20944/preprints202302.0204.v1

Table 1. Whole-rock and modal composition of lherzolite xenoliths.

Mode	HD5	HD6		HD24/2		HD34	HD38		HD58	HD68
Ol	64.0	55.4		58.6		58.9	57.3		55.7	61.0
Opx	21.0	23.0		28.9		22.7	23.1		25.8	25.0
Cpx	12.0	18.6		10.8		15.9	16.1		16.6	12.0
Spl	2.0	3.0		1.8		3.5	3.5		1.9	2.0
Center/ margin*	whole	center	margin	center	margin	whole	center	margin	whole	whole
SiO_2	44.20	44.30	44.50	45.94	44.55	44.27	44.68	44.77	44.70	44.11
TiO_2	0.08	0.17	0.16	0.10	0.10	0.17	0.17	0.16	0.15	0.10
Al_2O_3	2.24	3.99	3.63	3.04	3.21	3.75	4.09	3.80	3.27	2.89
Cr_2O_3	0.43	0.37	0.38	0.45	0.42	0.34	0.39	0.37	0.33	0.37
FeO*	8.16	8.54	8.37	7.62	7.78	8.5	8.01	8.09	8.20	8.22
MnO	0.17	0.14	0.15	0.13	0.13	0.13	0.14	0.14	0.16	0.15
MgO	40.90	37.32	38.16	39.86	40.96	38.45	38.26	38.80	39.00	40.36
CaO	2.77	3.52	3.38	2.53	2.39	3.28	3.52	3.23	3.24	2.55
Na_2O	0.44	0.42	0.46	0.26	0.30	0.39	0.32	0.35	0.35	0.24
K_2O	0.31	0.04	0.11	0.05	0.10	0.11	0.03	0.07	0.07	0.04
P_2O_5	0.02	0.02	0.02	0.02	0.03	0.02	0.02	0.02	0.02	0.01
NiO	0.26	0.23	0.23	0.27	0.28	0.24	0.24	0.26	0.24	0.26
L.O.I.	0.00	-0.44	-0.28	-0.28	-0.10	-0.14	0.01	0.13	-0.18	-0.16
Total	99.98	98.63	99.28	99.99	100.15	99.51	99.88	100.19	99.55	99.14
Rb (ppm)	3.604	0.352	1.181	0.607	1.571	1.323	0.308	0.761	0.801	0.577
Ba	47.00	6.15	15.67	3.06	19.20	8.9	5.05	7.61	6.60	7.70
Nb	1.320	0.116	0.526	0.120	0.346	0.15	0.169	0.177	0.123	0.131
K	2600	300	1000	400	800	900	200	600	600	300
La	1.650	0.820	1.163	1.025	1.360	0.91	0.374	0.468	0.730	0.558
Ce	3.390	1.835	2.995	1.972	2.100	1.88	0.997	1.008	1.740	1.460
Pb	0.145	0.134	0.525	0.209	0.307	0.131	0.205	0.392	0.231	0.192
Pr	0.380	0.260	0.454	0.215	0.254	0.262	0.163	0.168	0.259	0.158
Sr	40.15	21.26	30.78	18.53	22.25	20.05	15.98	16.68	34.76	11.35
Nd	1.420	1.286	2.127	0.894	1.010	1.231	0.873	0.956	1.244	0.737
Zr	10.82	10.28	11.92	6.10	5.96	9.72	7.20	7.74	7.38	4.75
Hf	0.196	0.361	0.363	0.141	0.214	0.332	0.230	0.280	0.278	0.160
Sm	0.330	0.430	0.618	0.244	0.285	0.404	0.364	0.351	0.386	0.247
Eu	0.120	0.167	0.227	0.093	0.094	0.160	0.150	0.134	0.147	0.095
Ti	514.0	1341.6	1331.2	593.0	573.0	1206.0	992.0	934.7	1038.2	767.3
Gd	0.353	0.577	0.703	0.356	0.355	0.6	0.543	0.526	0.475	0.370
Tb	0.066	0.113	0.124	0.063	0.068	0.109	0.106	0.101	0.091	0.066
Dy	0.434	0.792	0.847	0.432	0.509	0.764	0.718	0.684	0.614	0.479
Ho	0.092	0.176	0.181	0.101	0.107	0.166	0.164	0.153	0.129	0.106
Y	2.47	4.79	4.18	2.28	2.72	4.55	4.18	3.70	3.43	2.87
Er	0.285	0.545	0.527	0.319	0.350	0.47	0.490	0.463	0.381	0.330
Tm	0.041	0.077	0.078	0.047	0.050	0.075	0.076	0.070	0.053	0.048
Yb	0.264	0.498	0.513	0.325	0.380	0.488	0.512	0.493	0.335	0.329
Lu	0.042	0.083	0.079	0.052	0.058	0.078	0.082	0.075	0.055	0.052

* Analysis of center or margin of large xenoliths.

Preprints (www.preprints.org) | NOT PEER-REVIEWED | Posted: 13 February 2023 doi:10.20944/preprints202302.0204.v1

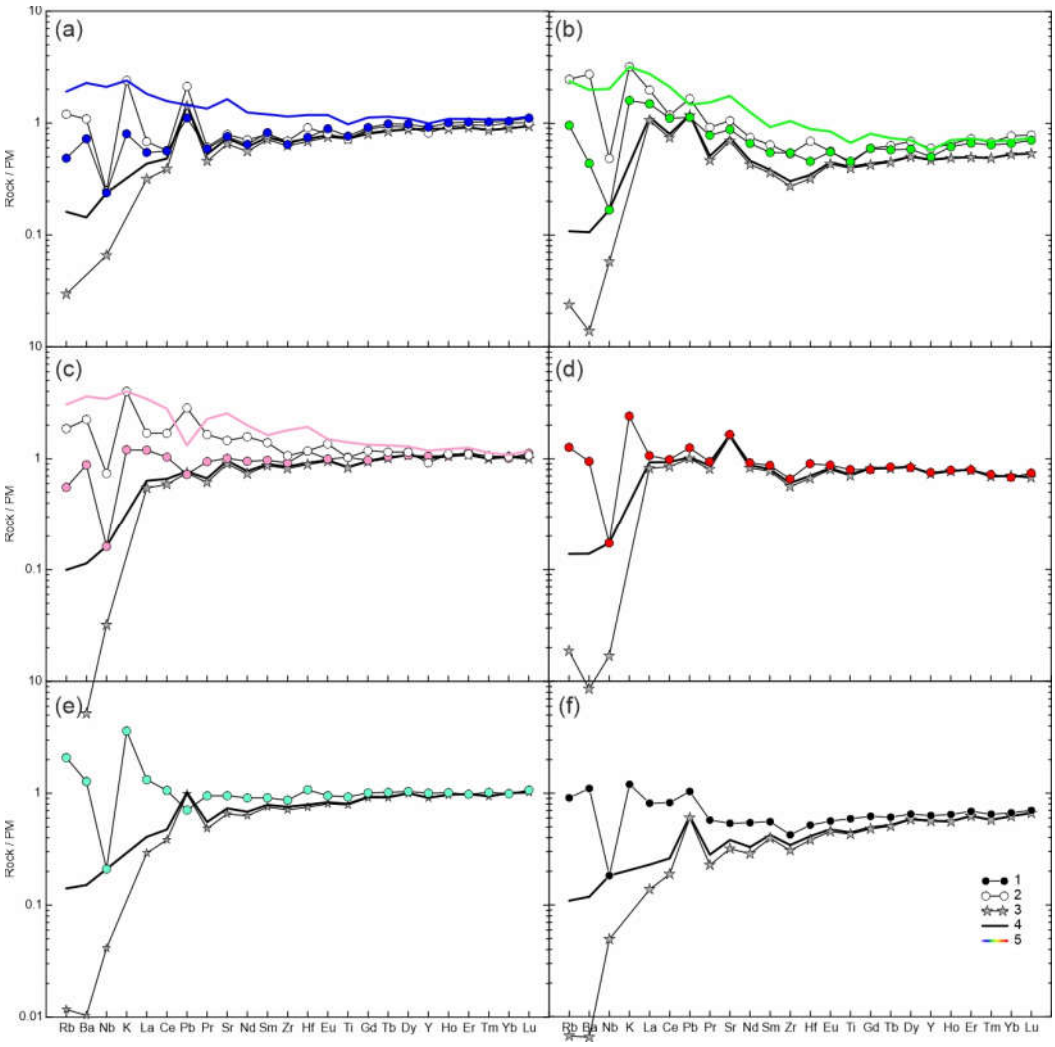

Figure 7. Measured and calculated trace element compositions of lherzolite xenoliths from Tumusun volcano. (**a**) HD38; (**b**) HD24/2; (**c**) HD6; (**d**) HD58; (**e**) HD34; (**f**) HD-68. 1 – measured whole-rock composition of central part of xenolith; 2 – measured whole-rock composition of marginal part of xenolith (only for a-c); 3 – calculated whole-rock composition obtained from modal composition and trace element abundances in olivine, ortho- and clinopyroxene; 4 – mix of calculated lherzolite compositions and basanite composition, with basanite proportion (x) defined by difference in Nb abundance between measured and calculated compositions; 5 – Mix of compositions of central part of lherzolite xenolith and basanite proportion (x) defined by difference in measured K abundance between the margin and center of xenolith.

3.4. Mineral trace element composition

The primary clinopyroxenes without reaction rims have two types of REE patterns. The first type is undifferentiated HREE-MREE and depletion in LREE, i.e., depleted pattern common for residual fertile lherzolites (Figure 8a). The normalized patterns of trace elements also show depleted shape and depletion in the most incompatible elements (from Ba to Nd) and weak minima of Ti and Zr (Figure 8b). Inside xenoliths, clinopyroxene with thin reaction zones have the same spectrum type and abundances of trace elements in Cpx1 (core) and Cpx2 (reaction rim), resembling composition of primary clinopyroxene without reaction rim, except for high Ba in Cpx2 (Figure 8d, e). In clinopyroxene grains located close to basanite/xenolith contact near to orthopyroxene reaction zone (Figure 8g, h) and at immediate contact with the basanite (Figure 8j, k), even Cpx1 has higher abundances of Ba and sometimes La and Ce but abundances of other trace element are similar to that of primary clinopyroxene. The composition of Cpx2 varies. Compared with Cpx1, Cpx2 has a gradual increase in trace element abundances toward the edge of reaction zone. In the internal part of reaction rim (Cpx2), the maxima of Ba, Sr and Eu appear, and

Preprints (www.preprints.org) | NOT PEER-REVIEWED | Posted: 13 February 2023 doi:10.20944/preprints202302.0204.v1

the minima of Zr, Hf, and Ti remain (Figure 8g-l; analyses #16, #8, #12). Further in the external part of reaction rim (Cpx2) higher trace element abundances combined with minima of Ba, Sr, and Eu are observed (Figure 8g-l; analyses #17, #13, #14). It is notable that Cpx1 from the smallest xenolith (1.5 cm in length) has depleted trace element pattern (Figure 9).

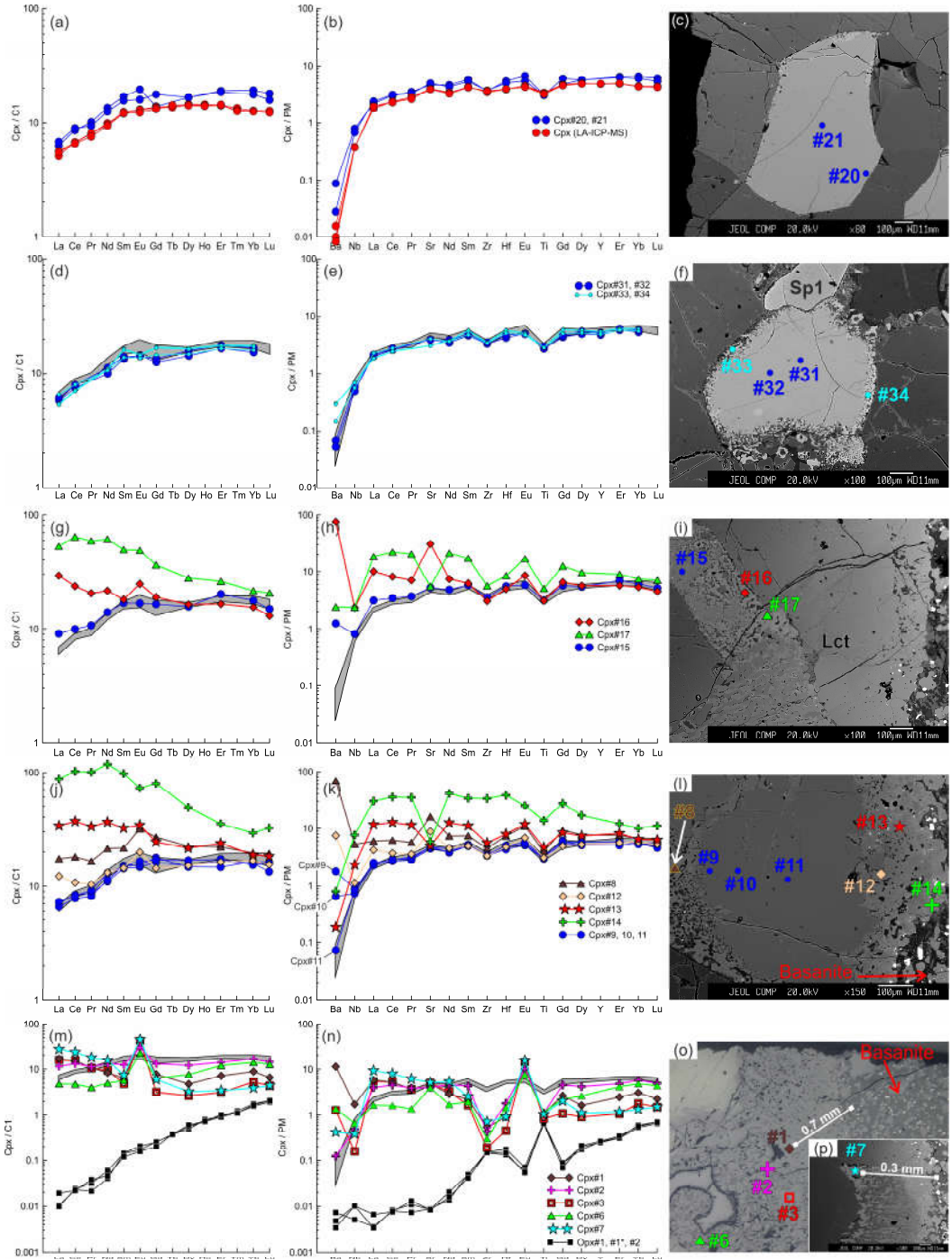

Figure 8. The trace element composition of the clino- and orthopyroxenes from sample HD38. (**a, b, c**) Primary clinopyroxene (#20, #21) without reaction rim. Trace element composition of primary clinopyroxene obtained by LA-ICP-MS is shown for comparison. (**d, e, f**) Cpx1 (#31, #32) with thin reaction rim of Cpx2 (#33, #34). Here and in d, e, g, h, j, k, m, n, the gray field shows the compositions of the primary clinopyroxene (#20, #21). (**g, h, i**) Cpx1 (Cpx#15) with wide reaction rim of Cpx2 (Cpx#16, Cpx#17) near the basanite/xenolith contact. (**j, k, l**) Cpx1 (#9 - 11) with wide reaction rim of Cpx2 (#12-14) at basanite/xenolith contact. (**m, n, o, p**) Cpx3 (#1-7) from orthopyroxene reaction

Preprints (www.preprints.org) | NOT PEER-REVIEWED | Posted: 13 February 2023 doi:10.20944/preprints202302.0204.v1

zone at basanite/xenolith contact. Location of primary orthopyroxene (#1, #1*, #2) is beyond the sample areas shown on photo.

Cpx1 from some of the samples is enriched in LREE both near the center of xenolith and at basanite/xenolith contact (Figure 10a, 11a). External parts of Cpx1 show more Ba near to the wider reaction rim (Figure 10e). Both Cpx1 and Cpx2 have similar REE patterns (Figure 10a, 10d, 11a). Cpx1 and Cpx2 normalized trace-element patterns demonstrate minima of Zr and Ti; Cpx1 shows minima of Ba and Nb but Cpx2 has maximum of Ba and sometimes Sr (Figure 10b, 10e, 11b).

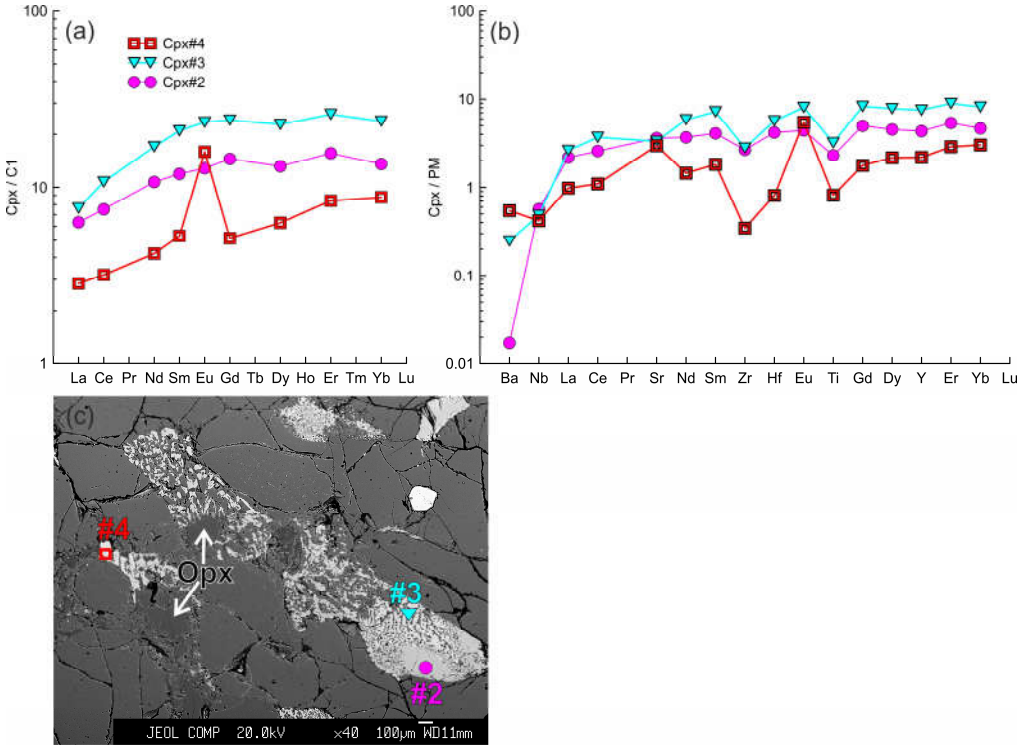

Figure 9. (a, b) The trace element composition of the clino- and orthopyroxenes from sample HD2 (xenolith of 1.5 cm in size). Cpx 1 (#2) with wide reaction rim of Cpx2 (#3) at the contact with orthopyroxene reaction zone. Cpx3 (#4) from reaction zone of Opx1. (**c**) Image showing different width of pyroxene reaction zones. Clinopyroxene located in upper right corner contacts with olivine only and shows narrow reaction rim.

In samples with LREE-enriched primary clinopyroxenes, Cpx3 is also enriched (Figure 10g, 11d, 11g). In samples with LREE-depleted primary clinopyroxene, Cpx3 can have both depleted (see Figure 9a) and enriched (see Figure 8m-o) trace-element pattern. In last case, the enriched Cpx3 is located at distance up to 1 mm from basanite/xenolith contact. Trace element abundances in Cpx3 vary from the levels close to that of primary clinopyroxene to values transitional between primary orthopyroxene and clinopyroxene (see Figure 8m- n, 9a-b, 10g-h, 11d-h). The general characteristic of Cpx3 is the presence of positive Eu anomaly and negative anomalies of Nb, Zr, Hf, and Ti. Anomalies of Ba and Sr are either positive or lack. Weak negative Eu anomaly was revealed only in Cpx3 from thin reaction rim of orthopyroxene located far from basanite/xenolith contact (Figure 11g). Notably, in the same orthopyroxene reaction zone there is Cpx3 with weak positive Eu anomaly. Moreover, Cpx3 from this reaction zone is distinct in higher REE abundances and minimum of Sr, compared to Cpx3 near to basanite/xenolith contact.

Preprints (www.preprints.org) | NOT PEER-REVIEWED | Posted: 13 February 2023 doi:10.20944/preprints202302.0204.v1

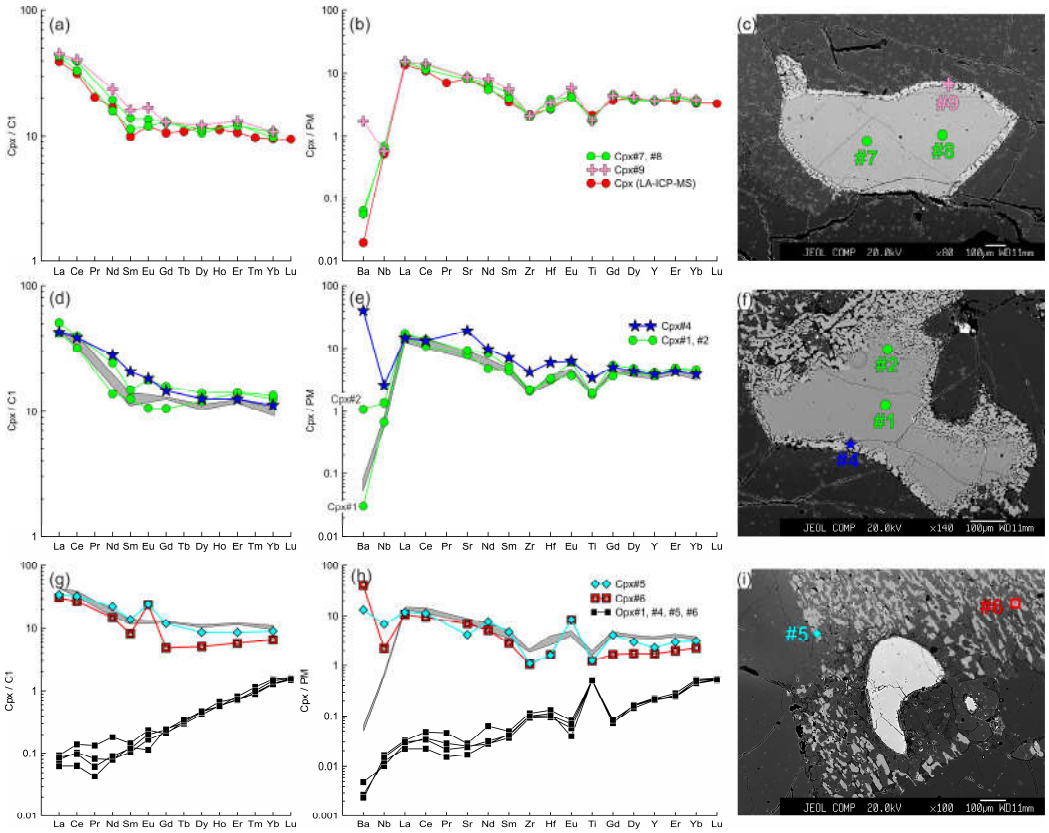

Figure 10. The trace element composition of the clino- and orthopyroxenes from sample HD24-2. (**a, b, c**) Cpx1 (#7, #8) with thin reaction rim of Cpx2 (#9) near the center of xenolith. Trace element composition of primary clinopyroxene obtained by LA-ICP-MS is shown for comparison. (**d, e, f**) Cpx1 (#1, #2) with wide reaction zone of Cpx2 (#4) near the basanite/xenolith contact. Here and in d, e, g, h, the gray field shows the compositions of Cpx1 (#7, #8). (**g, h, i**) Cpx3 (#5, #6) from orthopyroxene reaction zone located near basanite/xenolith contact. Location of primary orthopyroxene (#1, #4-6) is beyond the sample areas shown on photo.

Orthopyroxenes are LREE-depleted in the samples with depleted-type clinopyroxenes (see Figure 8 m). Orthopyroxenes in samples with LREE-enriched clinopyroxene show higher abundances of La and Ce compared to pattern common for depleted orthopyroxene (Figure 10g, 11d). On primitive-mantle-normalized plots, orthopyroxenes show maxima of Ti, Zr, Hf, complementary to corresponding minima in clinopyroxenes (Figure 8n, 10h, 11e). LREE-enriched orthopyroxenes show minima in Ba, Nb, and Sr (Figure 10h, 11e). In orthopyroxene with reaction zone of the second type, Opx1 has similar trace-element abundances and pattern as primary orthopyroxene from xenolith center, except for low abundances of Ba, La, Ce, and weak Eu maximum in the former (Figure 11j-l). At the same time, Opx1 preserves enriched type of REE pattern. Opx2 from this reaction zone has U-shaped normalized trace-element pattern with gradual decrease from HREE to Zr, Sm, Nd, and further growth in more incompatible elements, and is also characterized by maxima of Hf, Eu, and Ti (Figure 11j-l). Opx2 is enriched in highly incompatible elements, and have positive Eu anomaly and inhomogeneous composition, which is different from Opx1 in the same grain.

Preprints (www.preprints.org) | NOT PEER-REVIEWED | Posted: 13 February 2023 doi:10.20944/preprints202302.0204.v1

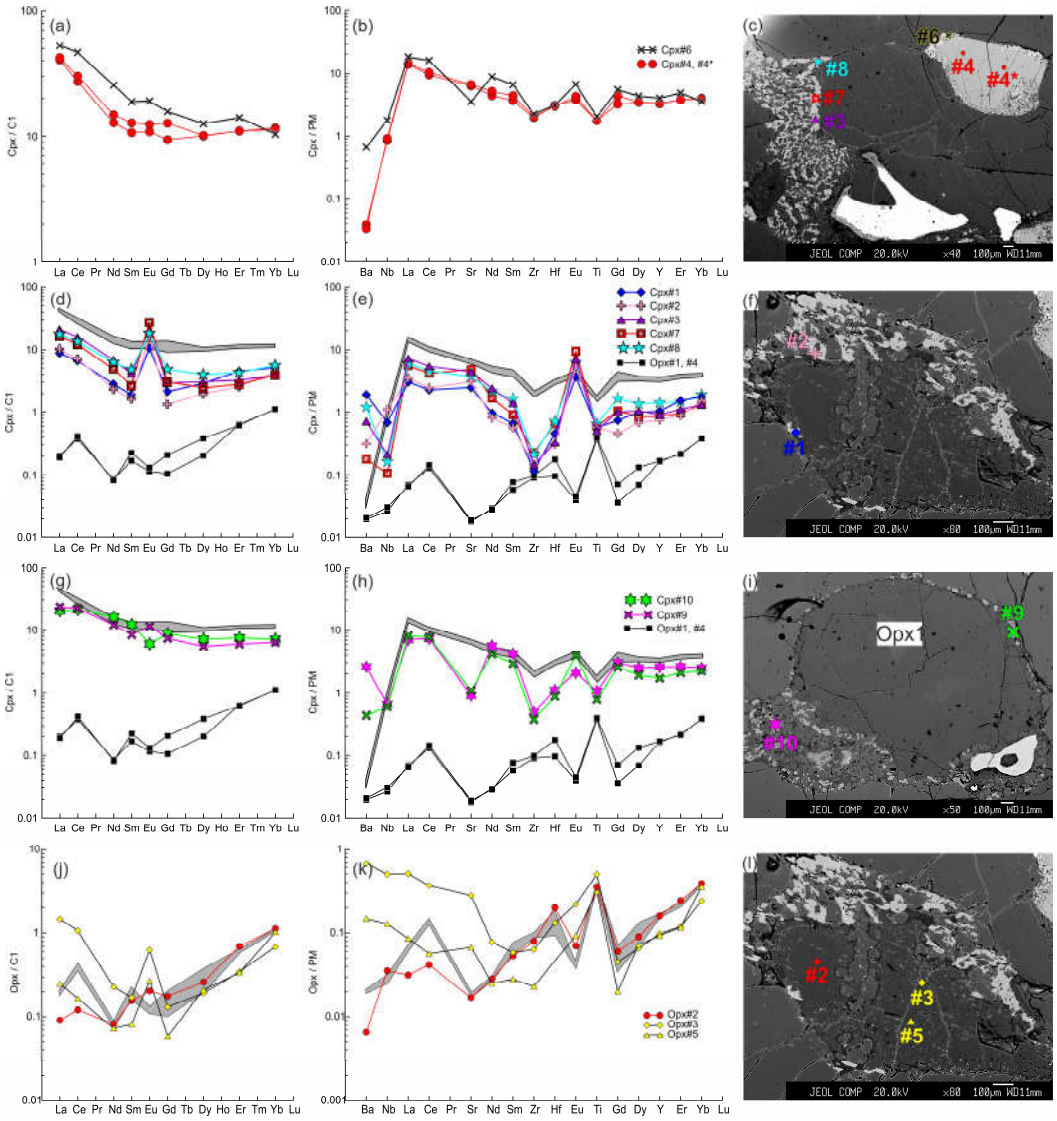

Figure 11. The trace element composition of the clino- and orthopyroxenes from sample HD5. (**a, b, c**) Cpx1 (#4, #4*) with wide reaction zone of Cpx2 (#6) near the contact with basanite. (**d, e, f**) Cpx3 (#1, #2 in f, #3, #7, #8 in c) from orthopyroxene reaction zone, and primary orthopyroxene (Opx#1, #4; the location is beyond the area shown on photo). Here and in g, h, the gray field shows the compositions of the Cpx1 (#4, #4*). (**g, h, i**) – Cpx3 (#9, #10) from thin reaction zone of Opx1 inside xenolith. (**j, k, l**) Orthopyroxene reaction zone of second type, with unreacted Opx1 (#2) and secondary Opx2 (#3, #5). The gray field shows the compositions of the primary orthopyroxene (#1, #4).

4. Discussion

4.1. Formation of reaction rims in minerals of lherzolite xenoliths of Tumusun volcano

Microstructural characteristics observed in the Tumusun peridotites are often found in peridotite xenoliths in alkaline basalts worldwide. However, the mineral reaction zones in xenoliths generally contain glasses, but not feldspar as in case of Tumusun lherzolites as found in [9] and present work. At the same time, in peridotite xenoliths from other localities the glasses of similar composition were described, including those with feldspar stoichiometry and MgO-free [23]. In peridotite xenoliths from Vitim volcanic field basanites (Baikal Rift Zone), feldspar (sanidine and plagioclase) is found along with rare segregations of glass (up to 10-20 μm) both in interstitial space and as inclusions in minerals [25]. In the studied Tumusun samples the largest vermicular aggregates found in mineral reaction zones are feldspar, and the rest aggregates are too small to be identified by petrographic methods. MgO was not detected and analyses yielded good stoichiometry, proving these aggregates to be feldspar. Also, Raman spectroscopy of several veinlets and

Preprints (www.preprints.org) | NOT PEER-REVIEWED | Posted: 13 February 2023 doi:10.20944/preprints202302.0204.v1

vermicular aggregates in reaction rims of orthopyroxene and clinopyroxene detects they are feldspars (Figure 6b), i.e., crystalline phases, but not the glass. The glasses of sanidine and anorthite composition [24] exhibit wide Raman bands (Figure 6b) and differ markedly from crystalline alkali feldspar and plagioclase whose characteristic Raman bands are narrow. The presence of feldspars (but not the glass) could be related to slow cooling. Thus, we can consider the feldspars of Tumusun peridotites as crystalized residual melts.

In studied samples, all minerals at basanite/xenolith contact have reaction rims. Toward the internal parts of the largest xenoliths, the mineral reaction zones gradually disappear (see Figure 2i). Therefore, the formation of mineral reaction zones could not be related to the mantle processes but takes place during transportation of xenoliths by the basanite magmas up to the surface. The reaction zones did not form during mantle metasomatism under influence of alkali-rich and water-poor fluid, as suggested by [9]. Inside xenoliths the secondary clinopyroxenes from reaction rims (Cpx2 and Cpx3) are characterized by low Al_2O_3, Al^{VI}/Al^{IV} ratio, and Na_2O, but higher Mg# and CaO than Cpx1 and primary clinopyroxene. The pressure calculations using single-pyroxene therbobatometer of [26] (equations 32a and 32d) show that Cpx1 and primary clinopyroxene exhibit similar pressure (1.5-1.7 GPa), while the secondary clinopyroxenes yield systematically lower pressures (0.1-1.85 GPa) than the primary clinopyroxenes (Electronic Supplementary Table S1).

This could be considered as evidence for the formation of reaction rims due to decompression melting of clinopyroxene during xenolith transportation to the surface [7]. Higher Cr# of secondary spinel of reaction zones, compared to the primary spinel, also could be a result of such melting. However, in the studied Tumusun lherzolites, the petrographic observations preclude the decompression melting, since not all grains and not all grain sides of clinopyroxene and spinel have reaction rims (see Figure 2e, 2j, 2k, 8c, 9c). In the case of Tumusun lherzolites the compositions of secondary minerals reflect the conditions of their formation under low (i.e., not mantle) pressure during transportation of xenoliths, but not decompression melting.

Inside xenoliths, the cores of clinopyroxene grains with reaction rims have the same major and similar trace element composition as clinopyroxenes without the reaction rim Moreover, Cpx2 of reaction rim also demonstrates similar trace element composition, except for high Ba and sometimes Sr (see Figure 5, 8a-e, 10a-e). This is possible only in case of dissolution of part of a clinopyroxene grain but not in case of partial melting, because in the second case there must be changes in composition of residual clinopyroxene according with the partition coefficients. The higher values of Ba and Sr in Cpx2 point at the presence of an interacting melt which dissolves clinopyroxene. Rarely observed orthopyroxene reaction zone of second type with the presence of Opx2 (see Figure 2c) is similar to the reaction rims of clinopyroxene. Opx2 is not residual because it has higher abundances of highly incompatible elements (including Nb) compared to Opx1. This reflects the participation of an additional melt in the formation of Opx2 (see Figure 11j-l). The process of dissolution (but not the melting) is confirmed by the lack of compositional changes in Opx1 relative to the primary orthopyroxene without reaction rims. The formation of Opx2-bearing reaction zone is possible due to incongruent dissolution of orthopyroxene in accordance to reaction Opx1+L2 → Opx2+L3.

The composition of secondary minerals of reaction zones in xenolith margins clearly reflects the basanite participation in their formation. For example, closer to the basanite/xenolith contact, Mg# of olivine (Ol2, Ol3, Ol4) and clinopyroxene (Cpx2, Cpx3) decreases to the values observed in corresponding basanite phenocrysts (Figure 3, 5). The above changes in Mg# occur in reaction zone of olivine, orthopyroxene, clinopyroxene at distance of ~100 to 200 μm from basanite/xenolith contact. Moreover, in rim of Cpx2 (with width of ~200 μm) contacting with basanite there is a considerable growth in trace elements toward the contact, which reflects diffusional exchange with the basanite (Figure 8j-l). Cpx3 at distance up to 1 mm from the contact is enriched in LREE (Figure 8m-o), although the primary pyroxenes of this sample have depleted REE pattern. Notably, all grains of Cpx3 have higher trace element abundances as compared to primary

 doi:10.20944/preprints202302.0204.v1

orthopyroxene, but lower than in Cpx2 at basanite/xenolith contact. This is possible if Cpx3 is formed from the melt whose composition is determined by composition of dissolving orthopyroxene and trace elements addition from basanite in accordance with diffusion coefficients.

Petrographic observations provide the evidence of melt circulation inside peridotite xenoliths and melt interaction with minerals. This is expressed in following: 1) reaction zone formation not around all sides of Opx, Cpx and Sp grains; 2) the reaction zones of clinopyroxene and spinel are wider in contact with orthopyroxene reaction zones (see Figure 2b; see Figure 9c); 3) occurrence of thin veinlets of feldspar (see Figure 2l). At the same time, inside xenoliths olivine is not zoned, i.e., its reaction zones lack. Therefore, the basanite melt doesn't penetrate inside lherzolite xenoliths, and the melt circulating inside xenoliths has a different composition. This follows from the composition of secondary minerals in reaction zones of minerals. Ol3 from orthopyroxene reaction zone is similar to that of primary olivine except for lower NiO in Ol3 (see Figure 3), and both Cpx2 and Cpx3 are more magnesian than primary clinopyroxene (see Figure 5). In clinopyroxene grain contacting with basanite, Ol4 from internal (at xenolith side) reaction zone already has Mg# as in primary olivine (see Figure 3, sample HD38). The trace element pattern of secondary clinopyroxene inside xenoliths is distinct from that of secondary clinopyroxene at basanite/xenolith contact. Cpx2 and Cpx3 of grains, located far from the contact inherit depleted or enriched type of REE distribution from primary pyroxenes of the sample.

Moreover, the composition of melt is changing inside xenoliths. This is reflected in varied mineral composition of orthopyroxene reaction zones (presence or absence of clinopyroxene), the difference of feldspar composition in reaction zones of different minerals, and wide variations of major-element compositions (Mg#, Al_2O_3, TiO_2, Cr_2O_3) of secondary clinopyroxenes. Even within a single reaction zone Cpx3 has wide variation in trace element abundances testifying the high heterogeneity of the parental melt. The melt is inhomogeneous because the xenolith-forming minerals (orthopyroxene, clinopyroxene, spinel) dissolve in different proportions therefore contributing different input into the composition of circulating melt.

Experimental studies of mechanisms of orthopyroxene dissolution in silica-undersaturated melts at 1 atm and 0.4 to 2 GPa [5,27] demonstrate that SiO_2-undersaturated melt produces incongruent dissolution of orthopyroxene to form silica- and alkali-rich melt followed by crystallization of high-magnesian olivine and clinopyroxene according to the reaction Opx1+L1 → Ol3+Cpx3+Sp+L2. The major-element composition of secondary olivine, clinopyroxene and alkali feldspar from orthopyroxene reaction zones of Tumusun peridotites agree well with these experimental data. Secondary minerals (Ol3, Cpx3 and Sp3) crystallize not from the host basanite melt but from newly-formed melt. The composition of the newly-formed melt is determined by composition of dissolving orthopyroxene and diffusion of elements (Ca, Al, Na and K) from basanite melt. Therefore, the secondary minerals are high-magnesian as the primary minerals of peridotites.

Based on experimental studies of peridotite–melt reaction at one atmosphere [5], a two-stage model was suggested to explain the development of sieve texture around clinopyroxene and spinel in mantle xenoliths. On the first stage, orthopyroxene undergoes incongruent dissolution to produce a melt rich in silica and alkalies, and olivine. On the second stage, this newly-formed melt migrates along grain boundaries and triggers incongruent dissolution of clinopyroxene and spinel [5]. As in the above experiments, the Tumusun lherzolites exhibit predominant development of clinopyroxene and spinel reaction rims in contact with orthopyroxene reaction zones and veinlets of alkali feldspar. At the same time, clinopyroxene and spinel grains also have reaction zones at basanite/xenolith contact. In the last case it is unclear, did these reaction zones form due to interaction with basanite, or before that during the reaction with a newly-formed melt (L2). The observed major-element compositions of secondary minerals from reaction zones and unreacted cores of clinopyroxene and spinel correspond to, and are explained by, the two-stage model.

Preprints (www.preprints.org) | NOT PEER-REVIEWED | Posted: 13 February 2023 doi:10.20944/preprints202302.0204.v1

4.2. Compositional changes in rocks due to the basanite-lherzolite interaction

Marginal and central parts of three large xenoliths have similar trace element patterns but the marginal parts demonstrate higher abundances of K_2O, LILE and sometimes LREE-MREE (Figure 7a-c).

To examine the possibility if the basanite input is responsible for this difference, the compositions of lherzolite-basanite mix have been calculated for these samples according to the formula (1):

$$M = x*B + (1-x)*L, \quad (1)$$

where M is mix, x is the basanite amount, B is basanite composition and L is composition of xenolith center.

The basanite amount (x) was calculated considering difference in K_2O in the central and marginal parts of samples. The calculated mix compositions are different from compositions of analyzed marginal parts for most trace elements except for Dy-Yb, which precludes the simple mixing of lherzolites with basanite (Figure7a-c).

To evaluate the possible gain of trace elements resulted from lherzolite-melt interaction, the compositions of 6 samples (3 large and 3 small xenoliths) were calculated using modal composition of the samples and measured composition of primary olivine, clinopyroxene and orthopyroxene. For all samples, including centers of large xenoliths, the measured and calculated compositions demonstrate similar (within analytical uncertainty) abundances of M-HREE, Nb, Zr, Hf, Ti. In contrast, abundances of Rb, Ba, and often LREE are lower in the calculated compositions than in the measured ones (Figure 7). There is a small difference in Nb between the calculated and measured compositions. Because Nb has low diffusion coefficient, this difference could be related to the input of basanite. To determine the basanite input, the composition of mix of calculated lherzolite and basanite was estimated from above formula using difference in Nb between the calculated and measured compositions of samples as proxy for basanite amount (x). The calculations demonstrate that xenoliths may contain up to 0.08-0.35% of basanite melt which apparently penetrates inside xenoliths along the cracks. But this mixing of lherzolite with basanite cannot explain the higher values of K, Rb, Ba, often LREE, and sometimes Sr in the measured compositions of lherzolites.

This inconsistency may be the result of diffusion at contact of two melts. The diffusion coefficients of mafic and felsic melts are the highest for LILE (correspondent to that of Ca), moderate for REE and minimal for HFSE [28,29]. Diffusion coefficients of REE decrease from La to Lu except Eu whose diffusion is faster than for the rest REE which relates to some amount of Eu^{2+} in the melt [29]. This explains the positive Eu anomalies in secondary Cpx3 of orthopyroxene reaction zones. Such positive Eu anomalies in the secondary clinopyroxenes from reaction rims are reported for peridotite xenolith from Cenozoic alkaline basalts in Xilong, South China [2], though generally the positive Eu anomaly in clinopyroxene is unusual.

The evidence for the diffusional input of trace elements is reflected in compositional changes of secondary Cpx3. Cpx2 located at basanite/xenolith contact show geochemical features common for clinopyroxene phenocrysts from alkaline basalts [30], such as trace element abundances and normalized trace element pattern, including negative anomalies of Ba, Nb, Sr, Ti. Cpx3 from orthopyroxene reaction zone located at distance of ~0.3 to 1 mm from basanite/xenolith contact is different from Cpx2 from the contact both in lower abundances and normalized pattern of trace elements. Therefore, this Cpx3 cannot crystallize directly from basanite melt. At the same time, Cpx3 has higher Mg# than the primary clinopyroxene. This suggests crystallization of Cpx3 from a melt formed due to orthopyroxene dissolution. Cpx3 shows higher abundances and different normalized pattern of trace elements (LILE- and LREE-enriched) compared to that of primary orthopyroxene which has depleted trace-element pattern. The values of Cpx/melt partition coefficients for REE vary and depend on melt composition (abundances of SiO_2 and Na_2O+K_2O), and could be higher than unity [31,32]. However, Cpx/melt partition coefficients for LREE

 doi:10.20944/preprints202302.0204.v1

are lower than for HREE, therefore to explain the observed LREE-enrichment in Cpx3, the parental melt has to be LREE-enriched. The abundances of Zr and Ti in Cpx3 are similar to, and Nb is higher compared to the composition of primary orthopyroxene (Figure 8m, n). Considering that Cpx/melt partition coefficients for Zr and Ti are less than unity and do not increase with increasing SiO2 content of melt (Vanucci et al., 1998), we can expect some gain of HFSE from basanite. Since diffusion coefficients for HFSE are lower than that for HREE (Holycross and Watson, 2016; Behrens and Hahn, 2009), one can also expect input of HREE in this process. This would not be observed if only primary orthopyroxene contributed to the trace-element budget of the melt. This suggests that not only LILE and LREE, but also some amount of HREE and HFSE was added from basanite to the melt from which Cpx3 was crystallized.

To summarize, the excess K, Na, Rb, Ba and excess LREE in measured whole-rock compositions are related to the formation of feldspars and secondary clinopyroxenes, respectively. This indicates non-isochemical interaction of lherzolites with basanite melt during transportation of xenoliths to the surface.

5. Conclusions

Lherzolite zenoliths from basanites of Tumusun volcano demonstrate mineral reaction zones which decrease in size from margins to the central parts of xenoliths until complete disappearance. Therefore, the mineral reaction zones in Tumusun lherzolites were formed as a result of interaction with host basanite during transport of xenoliths to the surface.

The influence of basanite melt on major- and trace-element composition of secondary minerals of reaction zones is notable only at distance up to 100-200 μm from basanite/xenolith contact. The composition of Cpx3 from orthopyroxene reaction zone at basanite/xenolith contact indicates its formation from a melt formed by dissolution of orthopyroxene and influenced by element diffusion from basanite melt. The major and trace element variations in Cpx3 testify melt heterogeneity. Inside xenoliths the secondary minerals from reaction zones have Mg# values equal to or higher than Mg# of corresponding primary minerals. The secondary clinopyroxenes inherit their depleted or enriched REE pattern from primary pyroxenes. In a single grain, Cpx2 has slightly higher LILE and similar abundances of other trace elements compared to unreacted central part of clinopyroxene.

The revealed rocks and mineral compositional features of the Tumusun lherzolite xenoliths agree well with two-stage reaction model of interaction between peridotite xenoliths and SiO_2-undersaturated alkaline basaltic melts, based on experimental data [5]. Our study implements this model by information on trace element behavior in this process. In xenolith margins at basanite/xenolith contact, orthopyroxene and probably clinopyroxene undergo incongruent dissolution to form new melt. The outer part of newly-formed melt is removed to the basanite, and internal part of the melt circulates inside of xenolith. The composition of newly-formed melt depends on composition of dissolving peridotite minerals and diffusion of elements from basanite melt in accordance with varying diffusion coefficients. Inside xenoliths, the newly-formed melt interacts with pyroxenes and spinel. This interaction results in dissolution of minerals and formation of reaction zones.

During the interaction process, the non-reacted central parts of minerals (pyroxenes and spinel) remain homogenous and have the same major- and trace-element composition as the primary lherzolite minerals. This finding allows using the compositions of the non-reacted central parts of minerals in small xenoliths to reconstruct the mantle stage of lherzolite formation. The REE patterns in clinopyroxene do not depend on xenolith size, and depleted and enriched spectra are found both in small and large xenoliths. Obviously, the REE patterns of primary clinopyroxenes is not influenced by the interaction of peridotites with the host basanites, but reflects preceding processes such as partial melting and mantle metasomatism.

The process of peridotite xenoliths interaction with the host basanite is not isochemical. Even the central parts of the largest xenoliths (whole-rock compositions) are enriched in Rb, Ba, K and sometimes La and Ce. Therefore, caution is need when using the whole-rock compositions for petrogenetic reconstructions, even for the largest xenoliths. It is also preferable to use whole-rock compositions calculated from minerals trace-element composition.

Supplementary Materials: Electronic Supplementary "Table S1".

Author Contributions: Conceptualization, M.A.G.; methodology, V.A.B. and A.A.K.; investigation, M.A.G.; data curation, A.B.P. and S.I.D.; writing—original draft preparation, M.A.G., V.A.B.; writing—review and editing, V.A.B. and A.A.K.; visualization, A.A.K.; supervision, M.A.G.; project administration, M.A.G.; funding acquisition, M.A.G., V.A.B. and A.A.K. All authors have read and agreed to the published version of the manuscript.

Funding: The study was funded by a grant from the Russian Science Foundation № 22-27-00821, https://rscf.ru/project/22-27-00821.

Data Availability Statement: The data supporting the findings of this study are available within the article and its supplementary materials.

Acknowledgments: The authors thank S. Simakin and E. Potapov for accurate and precise SIMS data of mineral trace element composition. I.S. Sharygin is thanked for providing access to Raman spectrometer.

Conflicts of Interest: The authors declare no conflict of interest. The funders had no role in the design of the study; in the collection, analyses, or interpretation of data; in the writing of the manuscript; or in the decision to publish the results.

References

1. Bonadiman, C.; Beccaluva, L.; Coltorti, M.; Siena, F. Kimberlite-like Metasomatism and 'Garnet Signature' in Spinel-Peridotite Xenoliths from Sal, Cape Verde Archipelago: Relics of a Subcontinental Mantle Domain within the Atlantic Oceanic Lithosphere? *Journal of Petrology* **2005**, *46*, 2465–2493, doi:10.1093/petrology/egi061.
2. Lu, J.; Zheng, J.; Griffin, W.L.; O'Reilly, S.Y.; Pearson, N.J. Microscale Effects of Melt Infiltration into the Lithospheric Mantle: Peridotite Xenoliths from Xilong, South China. *Lithos* **2015**, *232*, 111–123, doi:10.1016/j.lithos.2015.06.013.
3. Carpenter, R.L.; Edgar, A.D.; Thibault, Y. Origin of Spongy Textures in Clinopyroxene and Spinel from Mantle Xenoliths, Hessian Depression, Germany. *Mineralogy and Petrology* **2002**, *74*, 149–162, doi:10.1007/s007100200002.
4. Su, B.-X.; Zhang, H.-F.; Sakyi, P.A.; Yang, Y.-H.; Ying, J.-F.; Tang, Y.-J.; Qin, K.-Z.; Xiao, Y.; Zhao, X.-M.; Mao, Q.; et al. The Origin of Spongy Texture in Minerals of Mantle Xenoliths from the Western Qinling, Central China. *Contrib Mineral Petrol* **2011**, *161*, 465–482, doi:10.1007/s00410-010-0543-x.
5. Shaw, C.S.J.; Dingwell, D.B. Experimental Peridotite–Melt Reaction at One Atmosphere: A Textural and Chemical Study. *Contributions to Mineralogy and Petrology* **2008**, *155*, 199–214, doi:10.1007/s00410-007-0237-1.
6. Chattopadhaya, S.; Ghosh, B.; Morishita, T.; Nandy, S.; Tamura, A.; Bandyopadhyay, D. Reaction Microtextures in Entrapped Xenoliths in Alkali Basalts from the Deccan Large Igneous Province, India: Implications to the Origin and Evolution. *Journal of Asian Earth Sciences* **2017**, *138*, 291–305, doi:10.1016/j.jseaes.2017.01.028.
7. Pan, S.; Zheng, J.; Yin, Z.; Griffin, W.L.; Xia, M.; Lin, A.; Zhang, H. Spongy Texture in Mantle Clinopyroxene Recordsdecompression-Induced Melting. *Lithos* **2018**, *320–321*, 144–154, doi:10.1016/j.lithos.2018.08.035.
8. Ashchepkov, I.V. *Deep-seated xenoliths of the Baikal rift*; Nauka: Novosibirsk, 1991;
9. Ionov, D.A.; Prikhod'ko, V.S.; O'Reilly, S.Y. Peridotite Xenoliths in Alkali Basalts from the Sikhote-Alin, Southeastern Siberia, Russia: Trace-Element Signatures of Mantle beneath a Convergent Continental Margin. *Chemical Geology* **1995**, *120*, 275–294, doi:10.1016/0009-2541(94)00142-U.
10. Litasov, K.; Taniguchi, H. *Mantle Evolution beneath the Baikal Rift*; CNEAS monograph series ; Tōhoku Ajia Kenkyū Sentā sōsho ; dai 5-gō; Center for Northeast Asian Studies, Tohoku University: Sendai-shi, 2002; ISBN 978-4-901449-04-5.
11. Litasov, K.D.; Litasov, Y.D.; Malkovets, V.G. Metasomatism and Transformations of the Upper Mantle beneath the Southern Baikal Territory: Evidence from Xenoliths of the Bartoy Volcanic Area. *Geochemistry International* **2005**, *43*, 242–267.
12. Yarmolyuk, V.V.; Kovalenko, V.I.; Ivanov, V.G.; Pokrovskii, B.G. Magmatism and Geodynamics of the Southern Baikal Volcanic Region (Mantle Hot Spot): Results of Geochronological, Geochemical, and Isotopic (Sr, Nd, and O) Investigations. *Petrology* **2003**, *11*, 1–30.
13. Yarmolyuk, V.V.; Kovalenko, V.I.; Ivanov, V.G. Intraplate Late Mesozoic-Cenozoic volcanic province of Central-East Asia - projection of the hot mantle field. *Geotectonica* **1995**, 41–67.
14. Ivanov, A.V.; Demonterova, E.I.; He, H.; Perepelov, A.B.; Travin, A.V.; Lebedev, V.A. Volcanism in the Baikal Rift: 40years of Active-versus-Passive Model Discussion. *Earth-Science Reviews* **2015**, *148*, 18–43, doi:10.1016/j.earscirev.2015.05.011.

15. Makrygina, V.A.; Belichenko, V.G.; Reznitsky, L.Z. Types of Paleoisland Arcs and Back-Arc Basins in the Northeast of the Paleoasian Ocean (from Geochemical Data). *Russian Geology and Geophysics* **2007**, *48*, 107–119, doi:10.1016/j.rgg.2006.12.010.
16. Kovach, V.; Salnikova, E.; Wang, K.-L.; Jahn, B.-M.; Chiu, H.-Y.; Reznitskiy, L.; Kotov, A.; Iizuka, Y.; Chung, S.-L. Zircon Ages and Hf Isotopic Constraints on Sources of Clastic Metasediments of the Slyudyansky High-Grade Complex, Southeastern Siberia: Implication for Continental Growth and Evolution of the Central Asian Orogenic Belt. *Journal of Asian Earth Sciences* **2013**, *62*, 18–36, doi:10.1016/j.jseaes.2011.08.008.
17. Kotov, A.B.; Salnikova, E.B.; Reznitsky, L.Z.; Vasil'ev, E.P.; Kozakov, I.K.; Yakovleva, S.Z.; Kovach, V.P.; Berezhnaya, N.G. Age of Metamorphism of the Slyudyanka Crystalline Complex, Southern Baikal Area: U–Pb Geochronology of Granitoids. *Petrology* **1997**, *5*, 338–349.
18. Tsypukova, S.S.; Perepelov, A.B.; Demonterova, E.I.; Pavlova, L.A.; Travin, A.V.; Puzankov, M.Yu. Origin and Evolution of Neogene Alkali-Basaltic Magmas in the Southwestern Flank of the Baikal Rift System (Heven Lava Plateau, Northern Mongolia). *Russian Geology and Geophysics* **2014**, *55*, 190–215, doi:10.1016/j.rgg.2014.01.006.
19. Woodhead, J.D.; Hellstrom, J.; Hergt, J.M.; Greig, A.; Maas, R. Isotopic and Elemental Imaging of Geological Materials by Laser Ablation Inductively Coupled Plasma-Mass Spectrometry. *Geostand Geoanalyt Res* **2007**, *31*, 331–343, doi:10.1111/j.1751-908X.2007.00104.x.
20. Paton, C.; Hellstrom, J.; Paul, B.; Woodhead, J.; Hergt, J. Iolite: Freeware for the Visualisation and Processing of Mass Spectrometric Data. *J. Anal. At. Spectrom.* **2011**, *26*, 2508–2518, doi:10.1039/c1ja10172b.
21. Bottazzi, P.; Ottolini, L.; Vanucci, R.; Zanetti, A. An Accurate Procedure for the Quantification of Rare Earth Elements in Silicates. In Proceedings of the Secondary Ion Mass Spectrometry; Wiley: Yokohama, Japan, 1994; pp. 927–930.
22. Amosova, A.A.; Panteeva, S.V.; Tatarinov, V.V.; Chubarov, V.M.; Finkelstein, A.L. X-Ray Fluorescence Determination of Major Rock Forming Elements in Small Samples 50 and 110 Mg. *Analytics and control* **2015**, *19*, 130–138.
23. Wang, Y.; Han, B.; Griffin, W.L.; Zhang, L.; Shu, G. Post-Entrainment Mineral-Magma Interaction in Mantle Xenoliths from Inner Mongolia, Western North China Craton. *J. Earth Sci.* **2012**, *23*, 54–76, doi:10.1007/s12583-012-0233-x.
24. Matson, D.W.; Sharma, S.K.; Philipots, J.A. Raman Spectra of Some Tectosilicates and of Glasses along the Orthoclase-Anorthite and Nepheline-Anorthite Joins. *American Mineralogist* **1986**, *71*, 694–704.
25. Litasov, K.D.; Litasov, Y.D.; Mekhonoshin, A.S.; Malkovets, V.G. Mineralogy of Mantle Xenoliths from Pliocene Basanites of the Dzhilinda River (Vitim Volcanic Field). *Russian Geology and Geophysics* **2000**, *41*, 1534–1556.
26. Putirka, K.D. Thermometers and Barometers for Volcanic Systems. *Reviews in Mineralogy and Geochemistry* **2008**, *69*, 61–120, doi:10.2138/rmg.2008.69.3.
27. Shaw, C.S.J. Dissolution of Orthopyroxene in Basanitic Magma between 0.4 and 2 GPa: Further Implications for the Origin of Si-Rich Alkaline Glass Inclusions in Mantle Xenoliths. *Contributions to Mineralogy and Petrology* **1999**, *135*, 114–132, doi:10.1007/s004100050501.
28. Holycross, M.E.; Bruce Watson, E. Diffusive Fractionation of Trace Elements in Basaltic Melt. *Contrib Mineral Petrol* **2016**, *171*, 80, doi:10.1007/s00410-016-1289-x.
29. Behrens, H.; Hahn, M. Trace Element Diffusion and Viscous Flow in Potassium-Rich Trachytic and Phonolitic Melts. *Chemical Geology* **2009**, *259*, 63–77, doi:10.1016/j.chemgeo.2008.10.014.
30. Chen, P.; Fang, N.; Yuan, X. Geochemical Insights from Clinopyroxene Phenocrysts into the Magma Evolution of an Alkaline Magmatic System from the Sanshui Basin, South China. *Minerals* **2021**, *11*, 1295, doi:10.3390/min11111295.
31. Vannucci, R.; Bottazzi, P.; Wulff-Pedersen, E.; Neumann, E.-R. Partitioning of REE, Y, Sr, Zr and Ti between Clinopyroxene and Silicate Melts in the Mantle under La Palma (Canary Islands): Implications for the Nature of the Metasomatic Agents. *Earth and Planetary Science Letters* **1998**, *158*, 39–51, doi:10.1016/S0012-821X(98)00040-5.
32. Beard, C.D.; van Hinsberg, V.J.; Stix, J.; Wilke, M. Clinopyroxene/Melt Trace Element Partitioning in Sodic Alkaline Magmas. *Journal of Petrology* **2019**, *60*, 1797–1823, doi:10.1093/petrology/egz052.